Physics of Fluids

Subgrid scale modeling considerations for large eddy simulation of supercritical turbulent mixing and combustion

Cite as: Phys. Fluids **33**, 075112 (2021); https://doi.org/10.1063/5.0055751
Submitted: 02 May 2021 . Accepted: 24 June 2021 . Published Online: 19 July 2021

Umesh Unnikrishnan, Hongfa Huo, Xingjian Wang, and Vigor Yang

AIP Publishing

Physics of Fluids ARTICLE scitation.org/journal/phf

Subgrid scale modeling considerations for large eddy simulation of supercritical turbulent mixing and combustion

Cite as: Phys. Fluids **33**, 075112 (2021); doi: 10.1063/5.0055751
Submitted: 2 May 2021 · Accepted: 24 June 2021 ·
Published Online: 19 July 2021

Umesh Unnikrishnan,[1,a)] Hongfa Huo,[2,b)] Xingjian Wang,[3,c)] and Vigor Yang[1,d)]

AFFILIATIONS

[1]School of Aerospace Engineering, Georgia Institute of Technology, Atlanta, Georgia 30332, USA
[2]Pratt & Whitney, Hartford, Connecticut 06118, USA
[3]Department of Energy and Power Engineering, Tsinghua University, Beijing 10084, China

Note: This paper is part of the special topic, Tribute to Frank M. White on his 88th Anniversary.

[a)]umesh.aero@gatech.edu
[b)]hongfa.huo@gmail.com
[c)]xingjianwang@mail.tsinghua.edu.cn
[d)]**Author to whom correspondence should be addressed:** vigor.yang@aerospace.gatech.edu

ABSTRACT

This paper presents a systematic investigation of large eddy simulation (LES) and subgrid scale (SGS) modeling with application to transcritical and supercritical turbulent mixing and combustion. There remains uncertainty about the validity of extending the LES formalism developed for low-pressure, ideal-gas flows to simulations of high-pressure real-fluid flows. To address this concern, we reexamine the LES theoretical framework and the underlying assumptions in the context of real-fluid mixing and combustion. Two-dimensional direct numerical simulations of nonreacting and reacting mixing layers of gaseous methane and liquid oxygen in the thermodynamically transcritical and supercritical fluid regimes are performed. The computed results are used to evaluate the exact terms in the LES governing equations and associated SGS models. Order of magnitude analysis of the exact filtered and subgrid terms in the LES equations and *a priori* analysis of the simplifications are performed at different filter widths. It is shown that several of these approximations do not hold for supercritical turbulent mixing. Subgrid scale terms, which are neglected in the LES framework for ideal-gas flows, become significant in magnitude compared to the other leading terms in the governing equations. In particular, the subgrid term arising from the filtering of the real-fluid equation of state is shown to be important.

I. INTRODUCTION

In order to meet the ever-increasing demand for high efficiency and power output, there is a constant drive to increase the operating pressures of propulsion and energy-conversion systems. In these devices, fuel/oxidizer injection, mixing, and combustion typically occur at pressures and temperatures well over the critical states of both individual components and mixtures. Under such supercritical conditions, fluid mixing is diffusion-dominated, while under subcritical conditions two-phase interfacial dynamics prevail.[1–3] The present study offers specific recommendations for improved modeling of turbulent mixing in transcritical and supercritical fluid flows.

A number of experimental studies on transcritical and supercritical mixing and combustion have been carried out over the last three decades.[4–9] They have been constrained, however, by two factors—the challenges of replicating extreme operating conditions and the limited resolution of measurement techniques. Numerical modeling, on the other hand, while more capable in some ways, entails a wide array of challenges associated with nonideal thermodynamics, transport anomalies, and numerical techniques, in addition to the classical turbulence closure issues posed by fine-scale turbulent mixing and stiff chemical kinetics.[1,10] Fluid thermodynamic and transport properties vary rapidly near the critical point and require robust numerical schemes to accurately capture the physics. In addition, there are complexities for modeling of multicomponent mixtures, relevant to propellant mixing and combustion. Recent studies have shown that subcritical and phase separation phenomena can occur in some long-chain hydrocarbon–oxygen mixtures even when the operating pressure is supercritical with respect to the pure components.[11–13] The critical pressures of such mixtures are widely different and sometimes much higher than those of the constituent species, and the mixture undergoes transition through different thermodynamic regimes, depending on the local composition and pressure. Modeling approaches of real-fluid thermodynamics and numerical schemes have been considered in several works in the literature.[10,13–17]

Turbulence remains one of the most challenging unsolved areas of classical fluid mechanics. Direct numerical simulation (DNS), while most accurate, is limited to canonical flows at low Reynolds number and simple geometries, even with the currently available computing power. The challenge of grid resolution for DNS is particularly demanding in supercritical fluid flow simulation because of the inherently high Reynolds number associated with high liquid-like densities and low gas-like molecular viscosities.[1] Large eddy simulation (LES) is a powerful and promising alternative in the effort to gain fundamental understanding of the complex flow physics in this regime, and many LES studies have been devoted to supercritical mixing and combustion.[10,18–20] The LES formulation involves an array of modeling assumptions, and while these are reasonable under subcritical conditions, their validity in the transcritical and supercritical regimes has not yet been critically examined. Furthermore, the subgrid scale (SGS) models that were originally developed for ideal-gas flows have been applied directly to real-fluid flows without evaluation of their applicability and validity.

Subgrid scale modeling of the unresolved terms in the filtered equations is a central focus in the development of the LES framework. Several SGS models have been reported in the literature.[21] The first and still one of the most commonly used models was developed by Smagorinsky,[22] which uses a constant coefficient suggested by Lilly.[23] Further improvements were made by Germano *et al.*[24] and Lilly[25] who proposed the dynamic computation of the model coefficient based on the local flow features. Bardina *et al.*[26] introduced the scale-similarity model, which evaluates subgrid terms using test-filtered quantities. These different subgrid modeling strategies, along with others, have been used and compared for the simulation of supercritical turbulent mixing.[19,27,28] Most of the efforts in SGS modeling, however, have been focused on the unclosed terms in the momentum and energy conservation equations.

A common simplification made in the theoretical framework of LES is that the filtered values of secondary quantities (such as viscous stress, enthalpy, heat flux, and transport properties, including molecular viscosity, specific heat, thermal conductivity, and mass diffusivities), which are nonlinear functions of the primitive variables, are calculated directly from the resolved quantities using their original functional form. Because of the nonlinear nature of these constitutive relations (especially close to the critical point) and the filtering operation, such simplifications result in additional unclosed terms (analogous to the SGS stresses or energy flux). These terms, which will be derived mathematically in Sec. II C, represent the effect of subgrid scale fluctuations of each of the primitive variables and their mutual interactions, on the filtered flow quantity being evaluated. Since these terms are not computed directly in LES, they are often neglected, under the premise that they are of much lower order of magnitude as compared to the leading terms in the governing equation. While such assumptions seem to be reasonable and have been validated for ideal-gas flows, extension to transcritical and supercritical flow modeling introduces uncertainties. The issues with consistent filtering and the introduction of appropriate residual terms are also pertinent to the Reynolds-Averaged Navier-Stokes (RANS) methodology, which remains a widely used technique for scientific and engineering problems.

DNS serves as a useful tool for the development and assessment of SGS models for LES of turbulent flows and combustion,[29,30] but efforts in the context of supercritical mixing have been very limited. Selle *et al.*[28] performed an *a priori* study of the LES assumptions and SGS terms by means of DNS of supercritical temporal mixing layers. Some of the simplifying assumptions in LES, notably the modeling errors arising from the filtered pressure and heat flux in the momentum and energy conservation equations, were shown to be invalid in the supercritical fluid regime. Bellan[31] also conducted DNS of reacting temporal mixing layers at supercritical conditions. One limitation of these studies is that the characteristic Reynolds number was of the order of 1000, which does not adequately represent the behavior at small scales in realistic turbulent environments. Furthermore, the studies employed temporal mixing layer data, without consideration of the spatiotemporal evolution of the flow dynamics.

Ribert *et al.*[32] carried out a one-dimensional analysis of low- and high-pressure CH_4/O_2 premixed and nonpremixed flames. Their results indicated that computing the filtered pressure directly from the Favre-filtered species mass fractions and temperature leads to significant errors, especially in the transcritical regime. A correction for the filtered pressure was proposed in the tabulated framework. Since the study was based on a one-dimensional analysis with no realistic turbulence involved, the applicability of the proposed approach remains to be validated. Lapenna and Creta carried out DNS of supercritical and transcritical temporal jets.[33,34] They examined subgrid modeling errors associated with the evaluation of filtered thermodynamic properties and proposed a modeling approach using a presumed β-pdf distribution. Good improvement was achieved over the no-model approach. The work, however, was conducted at an initial jet Reynolds numbers of 1500/3000 and with a single species. The use of temporal jets inhibits a complete understanding of spatiotemporally evolving turbulence. A detailed assessment of the significance of these subgrid terms in multispecies turbulent flows at realistic Reynolds numbers is also yet to be undertaken.

A major challenge associated with DNS is the prohibitively high computational cost of resolving all the turbulent length scales. The cost typically scales as Re^3, and this limits the Reynolds number of the flows that can be investigated with the currently available computing power. Studying flows at low Reynolds number does not provide a true understanding of the physics of small-scale motion, due to the limited range of scales represented and lack of scale separation. Quasi two-dimensional DNS of supercritical mixing and combustion at Reynolds numbers of the order of 10^5 have been performed and investigated by Oefelein[35,36] and Ruiz *et al.*[37] Such studies allow a compromise between a realistic Reynolds number and computational feasibility and are essential to the evolution of a physical understanding and development of modeling strategies for practical applications.

In the present work, two-dimensional DNS of spatially evolving transcritical mixing layers, constituted by liquid oxygen (LOX) and gaseous methane at device-relevant conditions, is simulated and the database is used to conduct a systematic *a priori* analyses of the LES framework. The simulations are performed under both nonreacting and reacting conditions to investigate the effect of multispecies turbulent mixing and chemical reactions on the subgrid scale quantities of interest. In Sec. II of this paper, the theoretical formulation for DNS is presented and the governing equations for LES are derived from first principles to highlight the complete set of filtered and subgrid terms. An overview of the computational framework used to perform the simulations is provided in Sec. III. In Sec. IV, the filtered terms derived in Sec. II are computed exactly from the DNS database by explicit spatial filtering to assess the validity of the simplifying assumptions in the conventional LES framework. A budget analysis is performed by quantifying the order of magnitude of each of these terms to reveal the relative contribution of the terms with respect to the governing equations. The modeling errors associated with the computation of the filtered thermodynamic and transport quantities for multicomponent mixtures are investigated in detail at different filter widths.

II. THEORETICAL/MATHEMATICAL FORMULATION

In this section, the governing equations for the conservation of mass, momentum, energy, and species mass fraction, along with the real-fluid equation of state used in DNS are introduced. The LES filtered equations are then derived to highlight the unresolved subgrid terms in each of the governing equations. As an example, the formulation for the subgrid density, which results from the filtered equation of state, is shown in detail.

A. Conservation equations for DNS

The governing system of conservation equations and constitutive relations for a general fluid flow is represented as follows.

Mass:

$$\frac{\partial \rho}{\partial t}+\frac{\partial \rho u_j}{\partial x_j}=0. \tag{1}$$

Momentum:

$$\frac{\partial \rho u_i}{\partial t}+\frac{\partial\left(\rho u_i u_j+p\delta_{ij}\right)}{\partial x_j}=\frac{\partial \tau_{ij}}{\partial x_j}. \tag{2}$$

Energy:

$$\frac{\partial \rho E}{\partial t}+\frac{\partial(\rho E+p)u_i}{\partial x_i}=\frac{\partial(\tau_{ij}u_j+q_i)}{\partial x_i}. \tag{3}$$

Species mass fraction:

$$\frac{\partial \rho Y_k}{\partial t}+\frac{\partial \rho Y_k u_j}{\partial x_j}=\frac{\partial}{\partial x_j}\left(\rho D_k\frac{\partial Y_k}{\partial x_j}\right)+\dot{\omega}_k, \tag{4}$$

where $\rho,\ u_i,\ p,$ *and* Y_k are the density, velocity components, pressure, and mass fraction of species k, respectively, and $\dot{\omega}_k$ denotes the mass production rate of species k due to chemical reactions. The specific total energy E is defined as, $E=e+u_ju_j/2$, where e is the internal energy per unit mass and includes the sensible energy and the heats of formation of all the species in the given mixture. The specific enthalpy is defined as $h=(e+p/\rho)$ and the corresponding total specific enthalpy is $H=h+u_ju_j/2$. The viscous stress tensor τ_{ij} and the heat flux q_i are calculated as

$$\tau_{ij}=\mu\left(\frac{\partial u_i}{\partial x_j}+\frac{\partial u_j}{\partial x_i}\right)-\frac{2}{3}\mu\frac{\partial u_k}{\partial x_k}\delta_{ij}, \tag{5}$$

$$q_i=-\lambda\frac{\partial T}{\partial x_i}+\rho\sum_{k=1}^{N}h_kD_k\frac{\partial Y_k}{\partial x_j}. \tag{6}$$

In this formulation, Soret and Dufour diffusion effects are neglected in Eqs. (4) and (6), respectively, for the sake of simplicity, although the relevance of these terms remains an open question.[38] Once the reader is acquainted with the derivations and the unconventional subgrid terms that follow in Sec. II B, the filtered and subgrid components corresponding to other detailed transport terms can also be constructed and included in the formulation. All of the thermodynamic and transport properties, including dynamic viscosity μ, thermal conductivity λ, mass diffusivity of the kth species D_k, specific heat capacity c_p, and specific internal energy e and specific enthalpy h, are evaluated from fundamental thermodynamic theories,[14] and extended corresponding states principles.[39,40] The details of the theoretical formulation and implementation are presented by Meng and Yang.[14] The governing equations are solved by means of a preconditioning scheme with dual-time step integration.[41] In this numerical framework, the gauge pressure $p_g\ (=p-p_{ref})$, velocity components u, v, w, temperature T, and species mass fraction Y_k are treated as the primitive variables, and all secondary quantities are calculated from the primitive variables. For example, the density ρ is calculated from the Soave–Redlich–Kwong equation of state[42] (SRK-EOS), given as

$$p=\frac{\rho R_u T}{W-b\rho}-\frac{a\alpha}{W}\frac{\rho^2}{W+b\rho}. \tag{7}$$

This is a cubic equation of state, where a and b represent the molecular interactions. The above equation can be written as

$$p=\rho ZRT \tag{7a}$$

or

$$\rho=\frac{p}{ZRT}. \tag{7b}$$

Here Z is the compressibility factor that accounts for real-fluid effects.

B. Filtered equations and subgrid terms for LES

In LES, large-scale motions that carry most of the kinetic energy are fully resolved, while the effects of small unresolved scales, which are considered to be universal, are accounted for through SGS models. To separate large- and small-scale motions, a low-pass filtering operation is performed on the governing equations. In the present study, a box filter, defined as follows, is employed,

$$\bar{f}(\boldsymbol{x})=\frac{1}{\Delta V}\iiint_{dV} f(\boldsymbol{x})d\boldsymbol{x}. \tag{8}$$

Here, the filter size/volume used is the mesh size/cell volume of the corresponding LES computational grid. The Favre-filtered value of a flow variable is defined as

$$\tilde{f}=\frac{\overline{\rho f}}{\bar{\rho}}. \tag{9}$$

The LES equations are then derived by applying the Favre-filtering operation on the conservation equations (1)–(4) and assuming commutativity of the differential and filtering operations.

Mass:

$$\frac{\partial \overline{\rho(\mathbf{Q})}}{\partial t} + \frac{\partial\left(\overline{\rho(\mathbf{Q})}\widetilde{u}_j\right)}{\partial x_j} = 0. \tag{10}$$

Momentum:

$$\frac{\partial\left(\overline{\rho(\mathbf{Q})}\widetilde{u}_i\right)}{\partial t} + \frac{\partial}{\partial x_j}\left(\overline{\rho(\mathbf{Q})}\widetilde{u}_i\widetilde{u}_j + \overline{p}\delta_{ij}\right) = \frac{\partial}{\partial x_j}\overline{\tau_{ij}(\mathbf{Q})} - \frac{\partial}{\partial x_j}\overline{\rho(\mathbf{Q})}\left(\widetilde{u_i u_j} - \widetilde{u}_i\widetilde{u}_j\right). \tag{11}$$

Energy:

$$\frac{\partial\left(\overline{\rho(\mathbf{Q})}\widetilde{E(\mathbf{Q})}\right)}{\partial t} + \frac{\partial\left(\overline{\rho(\mathbf{Q})}\widetilde{H(\mathbf{Q})}\widetilde{u}_i\right)}{\partial x_i} = \frac{\partial}{\partial x_i}\left\{\widetilde{u}_j\overline{\tau_{ij}(\mathbf{Q})} + \overline{q_i(\mathbf{Q})} - \overline{\rho(\mathbf{Q})}\left(\widetilde{H(\mathbf{Q})u_i} - \widetilde{H(\mathbf{Q})}\widetilde{u}_i\right) + \left(\overline{u_i\tau_{ij}(\mathbf{Q})} - \widetilde{u}_i\overline{\tau_{ij}(\mathbf{Q})}\right)\right\}. \tag{12}$$

Species mass fraction:

$$\frac{\partial\overline{\rho(\mathbf{Q})}\widetilde{Y}_k}{\partial t} + \frac{\partial\left(\overline{\rho(\mathbf{Q})}\widetilde{Y}_k\widetilde{u}_j\right)}{\partial x_j} = \frac{\partial}{\partial x_j}\left(\overline{\rho(\mathbf{Q})D(\mathbf{Q})\frac{\partial Y_k}{\partial x_j}} - \overline{\rho(\mathbf{Q})}\left(\widetilde{Y_k u_j} - \widetilde{Y}_k\widetilde{u}_j\right)\right) + -\dot{\omega}_k(\mathbf{Q}). \tag{13}$$

The overbar and tilde denote the filtered and Favre-filtered quantities, respectively. The unclosed SGS terms that are generally considered in Eqs. (11)–(13), namely, the SGS stresses τ_{ij}^{sgs}, enthalpy flux H_i^{sgs}, viscous work σ_{ij}^{sgs}, and scalar flux Φ_{ij}^{sgs}, are defined as

$$\tau_{ij}^{sgs} = \overline{\rho(\mathbf{Q})}\widetilde{u_i u_j} - \rho\left(\widetilde{\mathbf{Q}}\right)\widetilde{u}_i\widetilde{u}_j, \tag{14}$$

$$H_i^{sgs} = \overline{\rho(\mathbf{Q})H(\mathbf{Q})u_i} - \rho\left(\widetilde{\mathbf{Q}}\right)H\left(\widetilde{\mathbf{Q}}\right)\widetilde{u}_i, \tag{15}$$

$$\sigma_i^{sgs} = \overline{u_j\tau_{ij}(\mathbf{Q})} - \widetilde{u}_j\tau_{ij}\left(\widetilde{\mathbf{Q}}\right), \tag{16}$$

$$\Phi_{kj}^{sgs} = \overline{\rho(\mathbf{Q})Y_k u_j} - \rho\left(\widetilde{\mathbf{Q}}\right)\widetilde{Y}_k\widetilde{u}_j. \tag{17}$$

Mathematically, these terms originate as the remnant from simplifying the filtered value of the product of the two quantities as the product of the corresponding filtered quantities. This is inevitable in the LES formulation, since complete information of the primitive variables at all the turbulent scales to compute the exact covariance terms is not available and hence has to be modeled. These terms qualitatively represent the effects of the interaction of flow quantities between the resolved scales and the unresolved subgrid scales, and accounting for them is essential to construct a true representation of the filtered flow field and turbulent statistics in an LES simulation. These terms are commonly modeled using the Smagorinsky model or its dynamic variants, employing an eddy-diffusivity hypothesis.

In the preconditioned formulation and solution approach, pressure and temperature are directly solved as part of the independent state vector, and density is calculated using the equation of state. In general, any secondary fluid property or flow quantity ϕ (ρ, E, H, c_p, $\tau_{ij,}$ D_k, etc.) is computed using the set of independent primitive variables, which in this case is $\mathbf{Q} = \{p, u, v, w, T, Y_k\}^T$, through the corresponding constitutive relation. We denote this relationship as $\phi = \phi(\mathbf{Q})$. In LES, the filtered value of ϕ is typically approximated as $\widetilde{\phi(\mathbf{Q})} \approx \phi(\widetilde{\mathbf{Q}})$, due to lack of complete information at all scales pertaining to $\mathbf{Q}$. The two terms in the approximation are not equal, as a consequence of the nonlinear nature of the functional form of ϕ with respect to the state vector and the filtering operation. The difference between $\phi\widetilde{(\mathbf{Q})}$ *and* $\phi(\widetilde{\mathbf{Q}})$ gives rise to additional terms in the governing equations as follows:

$$\rho^{sgs} = \overline{\rho(\mathbf{Q})} - \rho\left(\widetilde{\mathbf{Q}}\right), \tag{18}$$

$$(\rho H)^{sgs} = \overline{\rho(\mathbf{Q})H(\mathbf{Q})} - \rho\left(\widetilde{\mathbf{Q}}\right)H\left(\widetilde{\mathbf{Q}}\right), \tag{19}$$

$$\Delta\tau_{ij} = \overline{\tau_{ij}(\mathbf{Q})} - \tau_{ij}\left(\widetilde{\mathbf{Q}}\right), \tag{20}$$

$$q_j^{sgs} = \overline{q_j(\mathbf{Q})} - q_j\left(\widetilde{\mathbf{Q}}\right), \tag{21}$$

$$j_k^{sgs} = \overline{\rho(\mathbf{Q})D(\mathbf{Q})\frac{\partial Y_k}{\partial x_j}} - \rho\left(\widetilde{\mathbf{Q}}\right)D\left(\widetilde{\mathbf{Q}}\right)\frac{\partial\widetilde{Y}_k}{\partial x_j}. \tag{22}$$

There are also subgrid terms associated with evaluating the thermodynamic and transport properties from the filtered primitive variables. For ideal-gas flows, these contributions are usually smaller in magnitude than the other terms in the governing equations and can thus be neglected in the LES formulation. Recent studies,[28,33] however, have questioned the applicability of this assumption in the context of supercritical flows. Indeed, taking into account the nonlinear nature of thermodynamic non-idealities and resulting constitutive relations, it is important to include these additional terms for an accurate LES representation. Another factor contributing to the complexity of the LES modeling is the presence of the characteristic steep gradients of flow properties (in particular density) in transcritical and supercritical mixing.[38] These gradients play an important role in the dynamics of small-scale turbulence and alters the relative contributions and effects of subgrid terms.

To shed further light on these issues, the relevance of these terms is investigated by deriving the exact filtered conservation equations, including all of the terms. The magnitude of each term is evaluated using the DNS data. Expanding Eqs. (10)–(13) and using the definitions of the subgrid terms listed above, we have the following.

Mass:

$$\frac{\partial\overline{\rho(\mathbf{Q})}}{\partial t} + \frac{\partial\left(\rho\left(\widetilde{\mathbf{Q}}\right)\widetilde{u}_j\right)}{\partial x_j} + \frac{\partial\left(\rho^{sgs}\widetilde{u}_j\right)}{\partial x_j} = 0. \tag{23}$$

Momentum:

$$\frac{\partial\left(\overline{\rho(\mathbf{Q})}\widetilde{u}_i\right)}{\partial t} + \frac{\partial\left(\rho\left(\widetilde{\mathbf{Q}}\right)\widetilde{u}_i\widetilde{u}_j + \overline{p}\delta_{ij}\right)}{\partial x_j} + \frac{\partial\left(\rho^{sgs}\widetilde{u}_i\widetilde{u}_j\right)}{\partial x_j} = \frac{\partial}{\partial x_j}\left(\tau_{ij}\left(\widetilde{\mathbf{Q}}\right) + \Delta\tau_{ij} - \tau_{ij}^{sgs}\right). \tag{24}$$

Energy:

$$\frac{\partial\left(\overline{\rho(\mathbf{Q})}\widetilde{E(\mathbf{Q})}\right)}{\partial t}+\frac{\partial\left(\rho(\widetilde{\mathbf{Q}})H(\widetilde{\mathbf{Q}})\widetilde{u}_j\right)}{\partial x_j}$$
$$=\frac{\partial}{\partial x_j}\left(\widetilde{u}_i\tau_{ij}(\widetilde{\mathbf{Q}})+q_j(\widetilde{\mathbf{Q}})\right)+\frac{\partial}{\partial x_j}\left(\widetilde{u}_i\Delta\tau_{ij}+q_j^{sgs}-H_i^{sgs}+\sigma_{ij}^{sgs}\right)$$
$$+\frac{\partial\left((\rho H)^{sgs}\widetilde{u}_j\right)}{\partial x_j}. \tag{25}$$

Species mass fraction:

$$\frac{\partial\overline{\rho(\mathbf{Q})}\widetilde{Y}_k}{\partial t}+\frac{\partial\left(\rho(\widetilde{\mathbf{Q}})\widetilde{Y}_k\widetilde{u}_j\right)}{\partial x_j}$$
$$=\frac{\partial}{\partial x_j}\left(\rho(\widetilde{\mathbf{Q}})D(\widetilde{\mathbf{Q}})\frac{\partial\widetilde{Y}_k}{\partial x_j}+j_k^{sgs}-\Phi_{kj}^{sgs}\right)+\frac{\partial(\rho^{sgs}\widetilde{Y}_k\widetilde{u}_j)}{\partial x_j}+\overline{\dot{\omega}_k(\mathbf{Q})}. \tag{26}$$

Subgrid scale modeling issues associated with the chemical source term in Eq. (26) is a topic of wide research interest but is not considered further in this study. The above equations represent the general and exact form of the filtered equations including all subgrid terms.

C. Filtered equation of state and thermodynamic/transport property evaluation

In the above formulation, the ρ^{sgs} term appears most frequently. This term is closely examined in the present study. Application of the filtering operation on the equation of state (7a) yields

$$\bar{p}=\overline{Z\rho RT}=\bar{\rho}\widetilde{ZRT}=\bar{\rho}\widetilde{Z}\widetilde{R}\widetilde{T}+\bar{\rho}\left(\widetilde{ZRT}-\widetilde{Z}\widetilde{R}\widetilde{T}\right). \tag{27}$$

The second term on the right-hand side represents the subgrid pressure term that is often neglected in the LES formulation. Ribert *et al.*[32] examined the significance of this term at low- and high-pressure conditions using one-dimensional flames. In the above equation, R is the specific gas constant, defined as the universal gas constant R_u divided the molecular weight W of the mixture. For a multicomponent mixture with n species, R is calculated as

$$R=\frac{R_u}{W}=R_u\sum_{k=1}^{n}\frac{Y_k}{W_k}. \tag{28}$$

Combination of Eqs. (27) and (28) yields

$$\bar{p}=\bar{\rho}\widetilde{Z}\widetilde{T}R_u\sum_{k=1}^{n}\frac{\widetilde{Y}_k}{W_k}+\bar{\rho}R_u\left(\widetilde{ZT\sum_{k=1}^{n}\frac{Y_k}{W_k}}-\widetilde{Z}\widetilde{T}\sum_{k=1}^{n}\frac{\widetilde{Y}_k}{W_k}\right). \tag{29}$$

Even for ideal-gas flows ($Z=1$), the approximation of the covariance of the temperature and species mass fraction still leads to a subgrid term which is nonzero for multicomponent reacting flows.[43] The compressibility factor Z is further a nonlinear function of the state variables p, T, and $Y_i s$. Therefore, the direct evaluation or closure of the triple covariance term is nontrivial. In the LES formalisms currently used, it is difficult or impossible to obtain the value of the second term on the RHS of Eq. (27), because of the triple covariance term, which is not computed directly in LES. The second term, thus, remains unclosed and is often neglected in existing LES solvers. For supercritical and low-speed simulations, a pressure-based solution approach is often used to overcome numerical issues with spurious pressure oscillations and numerical instabilities.[14,44] In such cases, the equation of state is often implemented to calculate the density in terms of pressure and temperature as shown in Eq. (7).

The exact filtered density is given as

$$\overline{\rho_{exact}}=\overline{\rho(\mathbf{Q})}=\frac{\bar{p}}{\widetilde{ZRT}}. \tag{30}$$

In terms of Favre-filtered quantities, the filtered density is approximated as

$$\overline{\rho_{LES}}=\rho(\widetilde{\mathbf{Q}})=\frac{\bar{p}}{Z(\widetilde{\mathbf{Q}})R(\widetilde{\mathbf{Q}})\widetilde{T}}. \tag{31}$$

Using the DNS database, we can compute the exact and approximated filtered density by calculating the Favre-filtered quantities. The unclosed term, referred to as the subgrid density, can then be calculated as

$$\rho^{sgs}=\overline{\rho_{LES}}-\overline{\rho_{exact}}=\frac{\bar{p}}{Z(\widetilde{\mathbf{Q}})R(\widetilde{\mathbf{Q}})\widetilde{T}}-\frac{\bar{p}}{\widetilde{ZRT}}. \tag{32}$$

The relevance of this unclosed subgrid density is a primary focal point since it is coupled with multiple terms in the governing equations. An investigation of subgrid density was considered in the context of single-component temporal jets by Lapenna *et al.*,[44] but the significance and behavior would be drastically different for multicomponent flows. Analogous to the equation of state, there are subgrid terms associated with the evaluation of the filtered thermodynamic and transport properties in terms of the corresponding constitutive relations. These terms manifest primarily in the diffusive terms in the governing equations. For example, consider the approximation of the filtered heat flux term in the energy equation,

$$\frac{\partial}{\partial x_i}\overline{q_i(\mathbf{Q})}=\frac{\partial}{\partial x_i}\left(\overline{\kappa(\mathbf{Q})\frac{\partial T}{\partial x_i}}\right)$$
$$=\frac{\partial}{\partial x_i}\left(\kappa(\widetilde{\mathbf{Q}})\frac{\partial\widetilde{T}}{\partial x_i}\right)+\frac{\partial}{\partial x_i}\left(\overline{\kappa(\mathbf{Q})\frac{\partial T}{\partial x_i}}-\kappa(\widetilde{\mathbf{Q}})\frac{\partial\widetilde{T}}{\partial x_i}\right). \tag{33}$$

The second term on the right-hand side, which is a subgrid term, can be expanded further as

$$\frac{\partial}{\partial x_i}\left(\overline{\kappa(\mathbf{Q})\frac{\partial T}{\partial x_i}}-\kappa(\widetilde{\mathbf{Q}})\frac{\partial\widetilde{T}}{\partial x_i}\right)=\frac{\partial}{\partial x_i}\left(\overline{\kappa(\mathbf{Q})\frac{\partial T}{\partial x_i}}-\overline{\kappa(\mathbf{Q})}\frac{\partial\widetilde{T}}{\partial x_i}\right)$$
$$+\frac{\partial}{\partial x_i}\left(\left(\overline{\kappa(\mathbf{Q})}-\kappa(\widetilde{\mathbf{Q}})\right)\frac{\partial\widetilde{T}}{\partial x_i}\right). \tag{34}$$

In the equation above, the first term on the right-hand side represents the subgrid term associated with the expression of the covariance term as the product of two filtered quantities, while the second term represents the subgrid term associated with the evaluation of a Reynolds-filtered transport property in terms of the Favre-filtered state variables. A similar procedure can be applied for the other diffusive terms in

Eqs. (11)–(13) to yield the terms in (24)–(26). The subgrid terms associated with transport property evaluations are analyzed in Secs. IV A 1 and IV B 2 for the nonreacting and reacting flow cases respectively.

III. COMPUTATIONAL SETUP AND NUMERICAL METHOD

A. Computational domain and boundary conditions

To generate the database for the baseline DNS study, a canonical transcritical/supercritical planar mixing layer constituted of liquid oxygen (LOX) and gaseous methane streams co+flowing along a splitter plate is used, as shown in Fig. 1. This fundamental flow configuration is representative of many common applications, like fuel injectors, and has been widely studied.[37,45] The computational domain and flow conditions are adopted from a previous study.[46] Methane at 300 K is injected from the top of the splitter plate at a velocity of 60 m/s, while LOX at 120 K is injected from the bottom at a velocity of 10 m/s. The operating pressure is 100 bar, well above the critical pressures of methane and oxygen, and the resulting mixture at all compositions. The thickness of the splitter plate δ is 0.3 mm, comparable to the thickness of many injectors employed in propulsion engines. A plate length of 1 mm is included to account for the effect of the boundary layer development.

The computational domain extends to a distance of 10 mm downstream from the trailing edge of the plate and 5 mm in the transverse direction. A mean velocity profile following a one-seventh power law, superimposed with broadband fluctuations of 5% turbulence intensity, is used to simulate a fully developed turbulent boundary layer at the inlet for both incoming streams. No-slip boundary conditions are applied on the surface of the splitter plate. Outflow conditions are prescribed along the top and bottom boundaries. The Reynolds number based on the LOX density and viscosity, splitter plate thickness, and velocity difference across the plate is about 1.5×10^5.

B. Numerical schemes

A robust computational scheme is required to circumvent the numerical stiffness arising from rapid flow property variations and the wide range of characteristic time and length scales involved.[1,10] A unified treatment of general fluid thermodynamics, based on the concepts of partial-mass and partial-density properties, is established and incorporated into a preconditioning scheme.[14,41] All the thermodynamic properties, including the preconditioning matrix, Jacobian matrices, and eigenvalues, are derived directly from fundamental thermodynamics theories, producing a self-consistent and robust algorithm.[14] The numerical formulation can accommodate any equation of state and is valid for fluid flows at all speeds and at all fluid thermodynamic states. Further efficiency is achieved by employing temperature instead of enthalpy as the primary dependent variable in the preconditioned energy equation. This eliminates laborious iterations in solving the equation of state for temperature and consequently facilitates load balance among computational blocks in a distributed computing environment. The resultant scheme is highly efficient and suitable for parallel processing.

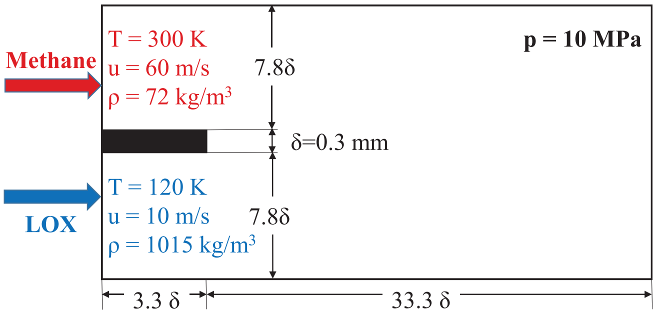

FIG. 1. Schematic of computational domain and flow conditions.

The numerical framework employs a finite-volume methodology, along with a dual-time step integration technique.[47] Temporal discretization is obtained using a second-order backward differencing scheme, and the inner-loop pseudo-time term is integrated with a four-step Runge–Kutta scheme. Spatial discretization is achieved with a fourth-order, central-difference scheme in generalized coordinates. A nine-point stencil is employed to evaluate the convective flux in each spatial direction to improve the spectral resolution of small-scale turbulence structures. Fourth-order matrix dissipation with a total-variation-diminishing switch developed by Swanson and Turkel[48] is applied to ensure numerical stability and minimize oscillations in regions with steep property variations.

Finally, a multiblock domain decomposition technique is employed to facilitate the implementation of parallel computing with message passing interfaces (MPI) at the domain boundaries. The parallelization methodology is robust and the speedup is almost linear. The numerical scheme used here is well established and has been applied to a variety of numerical studies of multiscale, multiphysics problems in the context of supercritical fluid and combustion dynamics, including the vaporization, mixing, and combustion of liquid droplets under transcritical and supercritical conditions,[49,50] cryogenic fluid injection,[51,52] and mixing and combustion in both shear coaxial and swirl injectors.[53–55]

C. Grid resolution

A total of about 19×10^6 grid cells is used for discretizing the present two-dimensional problem, including 2000 grid cells across the 0.3 mm rim of the splitter plate. This grid resolution is higher by a factor of 4 in each coordinate direction than that of a previous study using the same numerical framework by Huo and Yang.[46] In the recirculation zone downstream of the splitter plate, assuming a maximum turbulent velocity of $u' = 10\,\mathrm{m/s}$, the turbulent Reynolds number based on the local flow properties is about 1.6×10^4 with respect to the methane and 2.7×10^4 to the oxygen inlet flow conditions. The latter is taken to be the maximum Reynolds number for resolution considerations. The ratio of the largest to the smallest (Kolmogorov) length scales based on this Reynolds number is estimated to be $l_0/\eta = Re^{0.75} \approx 2000$. Considering the largest length scale to be of the order of magnitude of the plate thickness, $l_0 \approx 3 \times 10^{-4}$m, the order of magnitude of the Kolmogorov length scale is $\eta \approx 0.14\,\mu$m. The transverse grid spacing in the near field and along the center axis of the domain is about $0.15\,\mu$m. It should be noted that these estimates of local flow properties and turbulent velocities are the maximum values. In reality, the local Reynolds number would be at least one order of magnitude lower, due to the low velocity in the recirculation region and reduction in density of oxygen caused by mixing. For the reacting case, the Reynolds number is further lowered in the mixing layer due to thermal expansion caused by heat release and consequent reduction in density and increase in gas viscosity. Ruiz *et al.*[37] showed that resolving the plate thickness by 250 points was sufficient to obtain a converged spectrum for their benchmark DNS. Although their work considered a H_2/O_2 mixture, the operating conditions are close to our study. The spatial resolution in the mixing layer is, thus, deemed sufficient to resolve the entire range of turbulent length scales for both cases studied here.

The spectrum of turbulent kinetic energy is presented in Fig. 2 for the nonreacting case. The energy spectrum agrees well with the theoretical slope of $-5/3$ in the inertial subrange and starts to falloff at higher wave numbers. Figure 3 shows the transverse profiles of density and specific heat capacity for the nonreacting and reacting cases. The rapid property variations across the mixing layer in the transcritical regime are well resolved. Note that there exist regions where density varies by two orders of magnitude over a thickness on the order of 10 μm, which is well resolved by the grid. The characteristic length of such transition layers, defined as the ratio of the density difference and the maximum density gradient, is of the order of 10 μm for the nonreacting case,

$$l = \frac{\rho_{LOX} - \rho_{CH4}}{|\nabla \rho|_{max}}. \tag{35}$$

D. Combustion modeling

DNS of turbulent combustion requires the solution of appropriate chemistry mechanisms, often containing tens or hundreds of chemical species and reaction steps. These reaction processes and the resulting governing equations have to be solved on a grid that is sufficiently fine to resolve the length and time scales associated with the turbulence and flame. In addition, there are numerical issues posed by the inherent nonlinearity and stiffness of the resulting system of equations. For high-pressure combustion, an added computational cost is incurred with an evaluation of real-fluid thermodynamic and transport properties for multicomponent mixtures and high-pressure chemical kinetics. The computation of real-fluid properties alone has been shown to constitute over 50% of the total computational time.[56,57] For reacting flows with multispecies transport and detailed chemical kinetics, the computations associated with finite-rate kinetics would increase the computational complexity by an order of magnitude depending on the number of species and the reaction mechanism. Given these considerations, DNS of high-pressure combustion with finite-rate chemical kinetics is computationally prohibitive unless some simplifications are made.

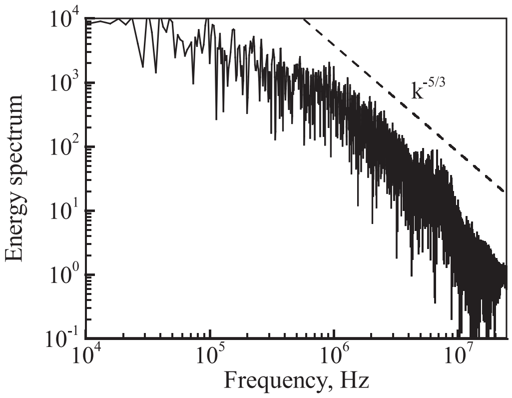

FIG. 2. Turbulent kinetic energy spectra in near field of splitter plate.

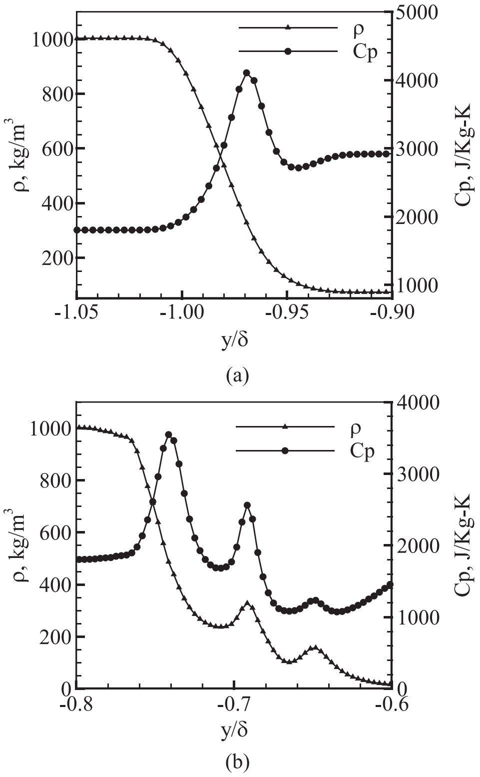

FIG. 3. Transverse profiles of density and specific heat capacity across the transition layer ($x/\delta = 5$) for the nonreacting (a) and reacting (b) flow cases.

To circumvent this problem, we use the laminar flamelet approximation to model the combustion process. The fundamental assumption of the flamelet model is that the reaction processes are infinitely fast compared to the fluid dynamic processes. In other words, the time scales of combustion are much smaller than the Kolmogorov scales. The flamelet concept is believed to be valid when the Karlovitz number, defined as

$$Ka = \frac{t_f}{t_\eta} \tag{36}$$

is smaller than 100.[58] The characteristic timescale of the flame can be calculated as

$$t_f = \frac{f_{st}^2(1 - f_{st})}{\chi_q}, \tag{37}$$

where f_{st} is the mixture fraction at the stoichiometric condition. For the LOX/methane mixture considered in this study, $f_{st} = 0.2$. The extinction (quenching) scalar dissipation rate χ_q is obtained from the solutions of counterflow diffusion flames of LOX and methane[59] and is found to be $3.6 \times 10^5\ \mathrm{s}^{-1}$ at the stoichiometric condition at 10 MPa. This gives a flame timescale of 7.1×10^{-8} s. The Kolmogorov timescale t_η, calculated from the Reynolds number, integral length scale, and reference velocity, is estimated to be of the order of 10^{-6}–10^{-7} s. The resulting Karlovitz number is thus of the order of 10^{-1}–10^{-2}, and the flamelet assumption is justified for the flow configuration considered in this study.

The length scale of a nonpremixed flame depends on the pressure and strain rate. The maximum strain rate in the current configuration for the nonreacting flow is found to be $6 \times 10^5\ \mathrm{s}^{-1}$. The corresponding laminar flame thickness is 20 μm, based on the half maximum width of temperature.[60] The mesh resolution in the flame zone is about 1–10 μm, which is smaller than the flame thickness. Although all the relevant turbulent and flame scales are resolved directly, the solution of finite-rate chemical kinetics is computationally prohibitive under these conditions, as previously discussed. Therefore, the laminar flamelet model is employed for the combustion modeling in our study. The coupling of flamelet-based models with DNS simulations has been considered in previous works[61,62] to overcome the computational challenges associated with detailed chemical kinetics. Mukhopadhyay *et al.*[63] have shown that the DNS combined with a

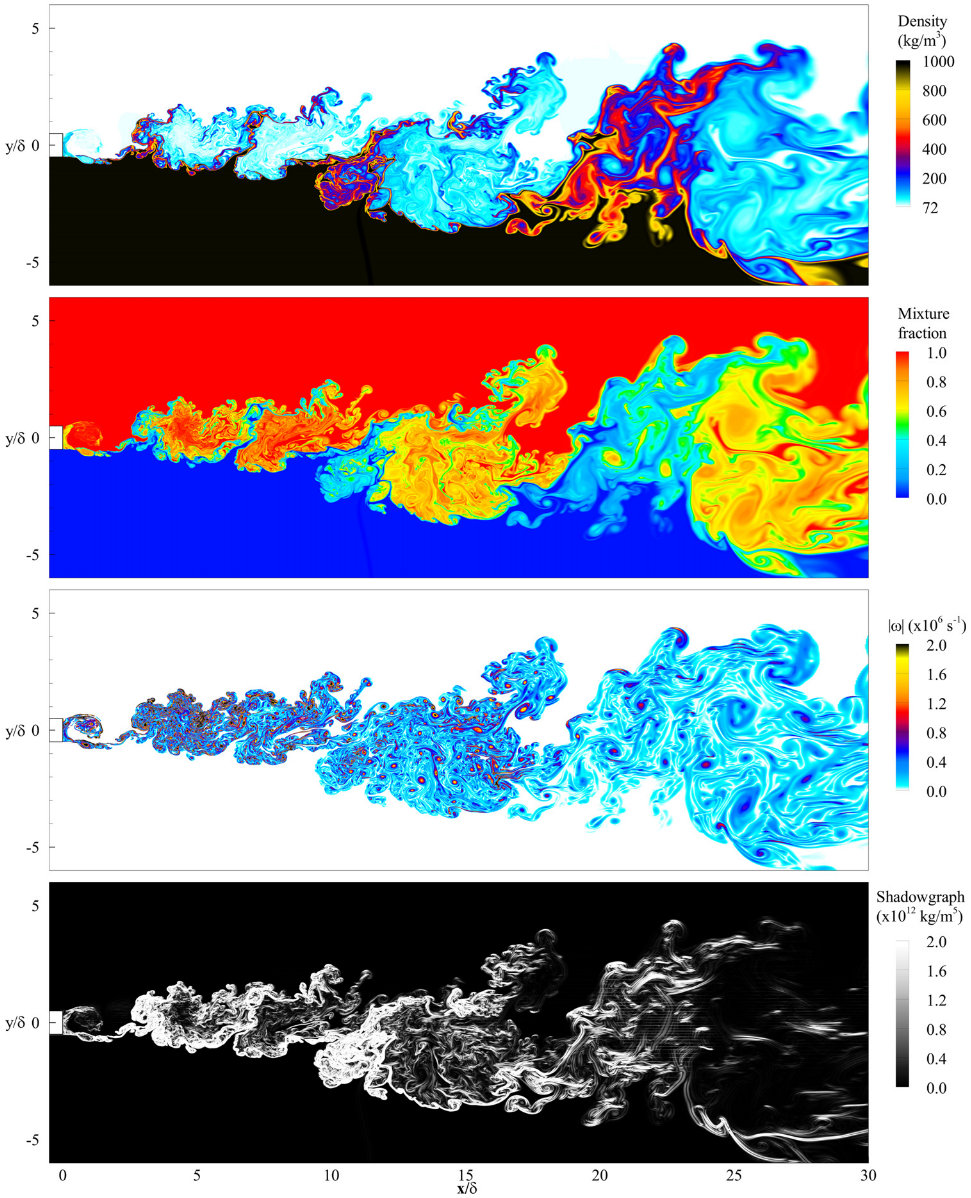

FIG. 4. Full-field instantaneous visualizations of nonreacting flowfield: distributions of density, mixture fraction and vorticity magnitude, and shadowgraph visualization (from top to bottom).

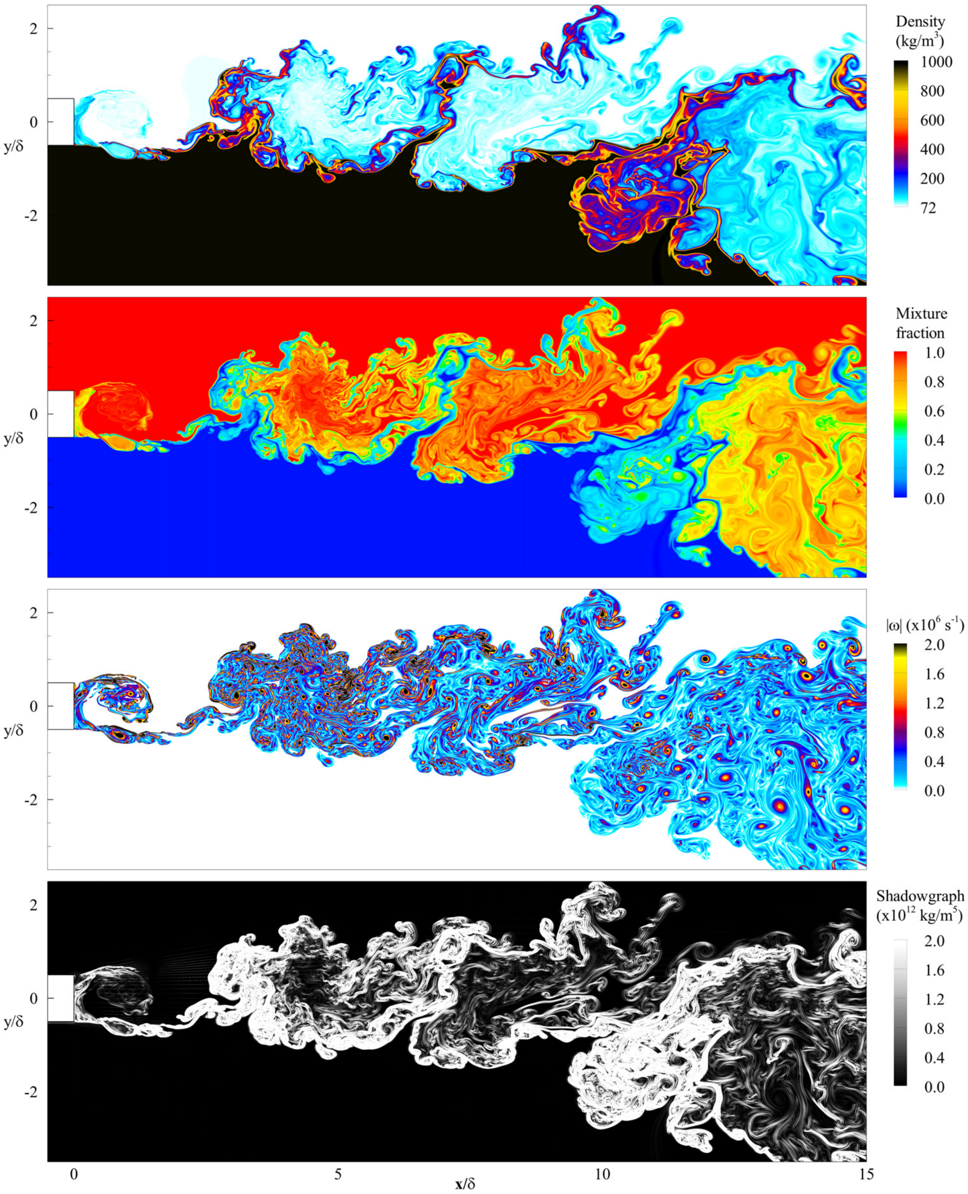

FIG. 5. Near-field instantaneous visualizations of nonreacting flowfield: distributions of density, mixture fraction and vorticity magnitude, and shadowgraph visualization (from top to bottom).

flamelet approach can reproduce exact DNS results when the grid size is of the order of the flame thickness.

The flamelet model implemented in this study uses precomputed laminar flamelet solutions obtained from simulations of one-dimensional counterflow diffusion flames that incorporate all real-fluid thermodynamics and validated chemical kinetics.[59,60] A reduced oxygen/methane mechanism by Sung *et al.*[64] is used to model the chemical reactions. The solutions are tabulated in a lookup table that is read by the computational fluid dynamics (CFD) solver. The mixture fraction (f) and scalar dissipation rate (χ) are used as input parameters, to obtain the species composition in every grid cell at each time step from the table. The flamelet solutions are only tabulated at a reference pressure corresponding to the prespecified operating condition, since the pressure fluctuations in the flow are within 1% of the reference pressure. For the DNS simulations, the conservation equation for the mixture fraction is given as

$$\frac{\partial \rho f}{\partial t} + \frac{\partial \rho u_j f}{\partial x_j} = \frac{\partial}{\partial x_j}\left(\rho D \frac{\partial f}{\partial x_j}\right). \tag{38}$$

The scalar dissipation rate is computed as

$$\chi = 2D\left(\frac{\partial f}{\partial x_j}\right)^2, \tag{39}$$

where the diffusivity D is estimated from the mixture thermal conductivity with the assumption of unity Lewis number. Accurate modeling of real-fluid mass diffusivities could play a key role in determining the flame characteristics as shown by Guven and Ribert.[45] It is emphasized here, that the primary focus of this work is to investigate inconsistencies associated with LES filtering and subgrid modeling at supercritical conditions. The flamelet model offers a computational balance to obtain a representative fully resolved multispecies reacting flow field upon which these issues can be clarified.

IV. RESULTS AND DISCUSSION

A. Nonreacting flow (supercritical turbulent mixing)

1. Instantaneous nonreacting flowfield

Instantaneous snapshots of the full and near flowfields for the nonreacting mixing case are shown in Figs. 4 and 5, respectively, in terms of distributions of density, mixture fraction, and vorticity magnitude, along with a simulated shadowgraph image (magnitude of second derivative of density). The pressure fluctuations in the flowfield remain within 1%–2% of the operating pressure, and above the critical pressure of the mixture at all times. No distinct interface is observed between the liquid oxygen and methane stream, as the surface tension and enthalpy of vaporization go to zero across the critical mixing temperature. Strong vortices develop due to the velocity difference, and stringy, fingerlike structures appear along the liquid oxygen stream. The mixing layer shows behaviors similar to classical variable-density fluid mixing, as observed in the experiments of Chehroudi *et al.*[6] Another important observation from the density and shadowgraph images is the rapid variation of density and resulting steep density gradients across the mixing layer. The high-density gradient regions are a characteristic feature of transcritical and supercritical mixing flows and are highlighted in the shadowgraph visualizations. As the LOX stream, which is initially at a subcritical temperature of 120 K, meets the warmer gaseous methane stream downstream of the splitter plate, its temperature increases and it goes through a transcritical regime, where thermodynamic and transport properties are known to be very sensitive to changes in pressure and temperature. This poses a severe challenge in accurately resolving the flow variations, especially at the smallest turbulent scales. The rapid variation of properties across the mixing layer and the imposed grid resolution in LES have an impact on the magnitude of the subgrid terms and are important considerations for accurate SGS modeling.

Figure 6 shows the flow evolution through instantaneous snapshots of density at various time instants. The spatial and temporal motions of the fine turbulent scales are captured in very high detail. Such a high-resolution spatiotemporal DNS database facilitates a systematic examination of the accuracy of fluid property evaluation using the filtered variables $(\overline{\phi(\mathbf{Q})} \sim \phi(\widetilde{\mathbf{Q}}))$ and other SGS terms. In Secs. IV A 2 and IV A 3, LES filter sizes of $\overline{\Delta} = 10\Delta_{DNS}$ (corresponding to an approximate mesh size of 1.5 μm, or 4–8 points across the characteristic length of the transition layer) and $\overline{\Delta} = 20\Delta_{DNS}$(corresponding to a mesh size of about 3 μm, or 2–4 points across the characteristic length of the transition layer) are applied to the DNS dataset to obtain the terms in the LES governing equations.

2. Modeling errors in computation of filtered flow properties

In LES, the filtered thermodynamic and transport properties are calculated directly from resolved primitive variables without including the effect of the SGS fluctuations of those variables. With the DNS database, it is possible to explicitly quantify the uncertainties introduced by this approximation and use that information to guide the development of LES modeling strategies. For any fluid property ϕ, the relative modeling error can be defined as

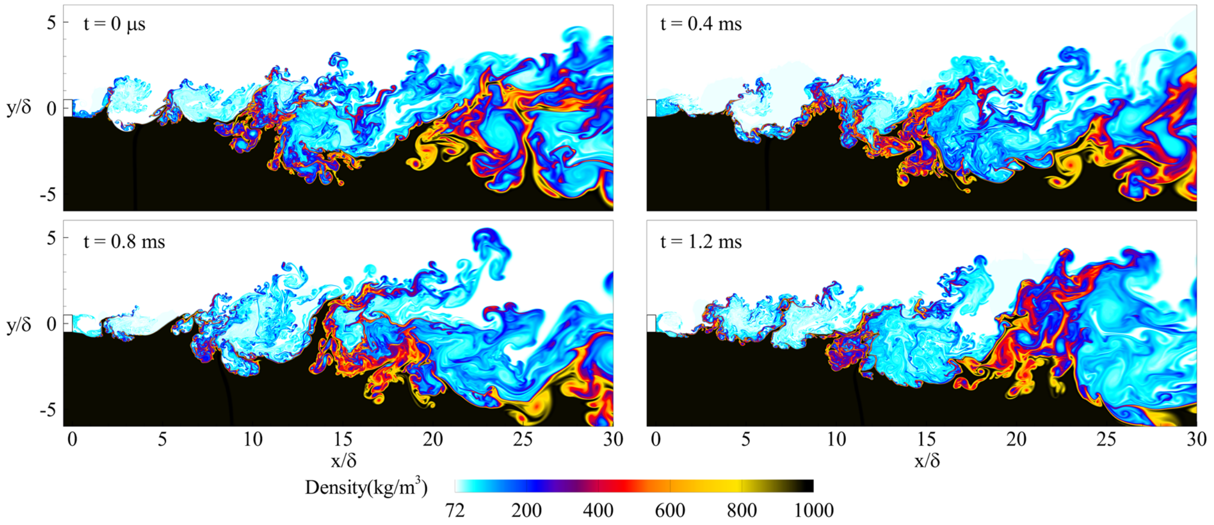

FIG. 6. Spatiotemporal evolution of the density field at various time instants.

$$\varepsilon_{\phi} = \frac{\overline{\phi(\mathbf{Q})} - \phi(\widetilde{\mathbf{Q}})}{\overline{\phi(\mathbf{Q})}}. \tag{40}$$

Figures 7 and 8 show the scatterplot of the relative errors in computing the filtered density, specific heat capacity, specific enthalpy, dynamic viscosity, thermal conductivity, and mass diffusivity of methane as functions of mixture fraction for filter size $\overline{\Delta} = 10\Delta_{DNS}$ and $20\Delta_{DNS}$, respectively. The errors are significant for most of these properties, with regions where error is as large as 20% for density and specific heat and over 50% for species mass diffusivity. The spatial distributions of the relative error magnitudes are shown in Figs. 8 and 9. The error occurs mainly in the transcritical interface between the LOX and methane streams (within 10^{-5} m). Through the transition layer, density drops rapidly from 1015 to about 75 kg/m^3, and c_p varies by a factor of 2 as shown in Fig. 3. This level of variation is generally not fully resolved on the scale of the LES filter. The filtered properties are misrepresented when calculated directly from the Favre-filtered variables without taking into account the associated SGS fluctuations. The definition of Favre-filtering, which is essentially a density-weighted averaging, dictates that the values of Favre-filtered quantities would be skewed toward the denser species, depending on the local species distribution. In this case, the Favre-filtered temperature and species mass fraction are primarily biased toward that of oxygen. This contributes to the difference between the exact filtered property $\overline{\phi(\mathbf{Q})}$ and the corresponding property evaluated from Favre-filtered state variables $\phi(\widetilde{\mathbf{Q}})$. Such difference has been shown to exist even for the computation of filtered pressure in the ideal-gas equation of state for compressible, multicomponent flows by Ribert *et al.*[43] The percentage deviation is much more significant in this case, due to the strong nonlinearity in the state relationships under the transcritical and supercritical conditions.

The sign of the error for a property would depend, in general, on the value of the corresponding property of the denser species relative to the lighter species. For example, we find that the approximated filtered density is over-estimated and the error is negative, because of the higher density of the low-temperature LOX stream. Similarly, the specific enthalpy and species diffusivity of oxygen are much lower than that of methane, and the corresponding filtered values are also under-estimated, resulting in a positive error. These three properties are strong functions of temperature and species composition and vary by over two orders of magnitude across the mixing layer. Consequently, the magnitude of error in the filtered property calculation is relatively higher. In contrast, the behavior is slightly different for the other three properties, which are relatively weaker functions of temperature. These properties vary at most by one order of magnitude and the variation is mostly across the transcritical interface of the mixing layer. The error distributions of these properties exhibit both positive and negative values in different regions. In reality, the evaluation of properties depends on the instantaneous species concentrations, temperature, and pressure, which are influenced by the flow evolution and turbulent mixing of the streams. The situation becomes even more complex in the case of reacting flows with several intermediate species and stronger variations in temperature and species concentrations.

The scatterplot of relative errors and the corresponding error distribution for a coarser filter size $\overline{\Delta} = 20\Delta_{DNS}$ are shown in Figs. 8 and 10, respectively. As the filter size is increased, the amount of information of subgrid fluctuations that is filtered out increases. As a result, there is wider deviation between exact- and Favre-filtered flow variables. This trend is shown in the figures, where the overall errors in property estimation increase in terms of both the range of the maximum errors and the density of points with higher errors. This trend can be visualized more clearly by comparing with Fig. 10. While these results quantify the errors with respect to the individual thermodynamic and transport properties, it is essential to understand and evaluate how these errors manifest with respect to the actual terms in the governing conservation equations. This is done through a systematic

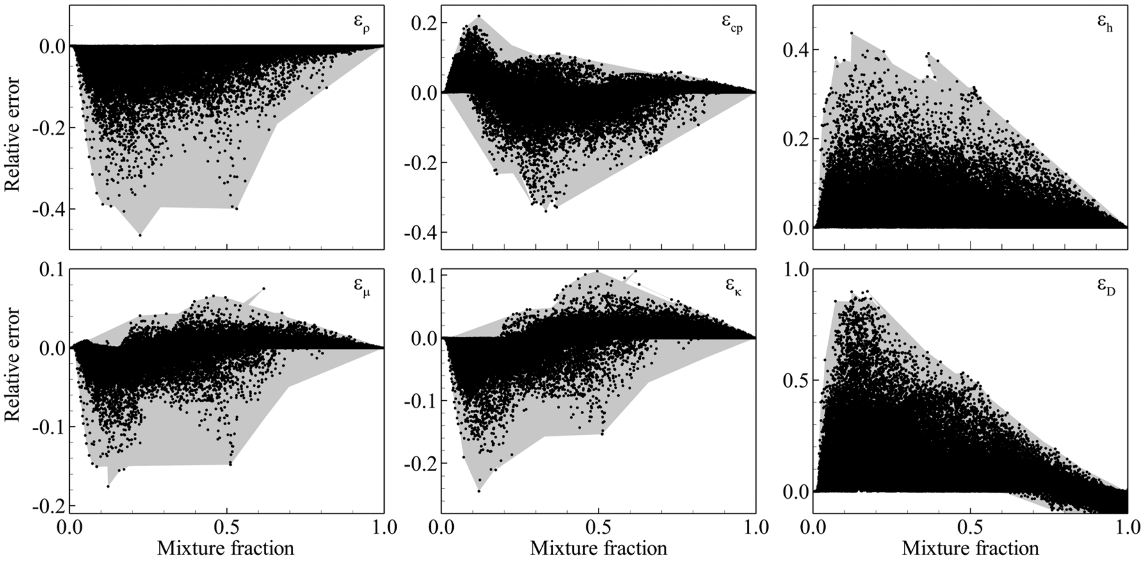

FIG. 7. Relative errors in filtered property calculations as a function of mixture fraction. $\varepsilon_{\phi} = (\overline{\phi(\mathbf{Q})} - \phi(\widetilde{\mathbf{Q}})/\overline{\phi(\mathbf{Q})})$. (Top) density, specific heat capacity, and specific enthalpy, (bottom) dynamic viscosity, thermal conductivity, and mass diffusivity of methane, $\overline{\Delta} = 10\Delta_{DNS}$ (nonreacting).

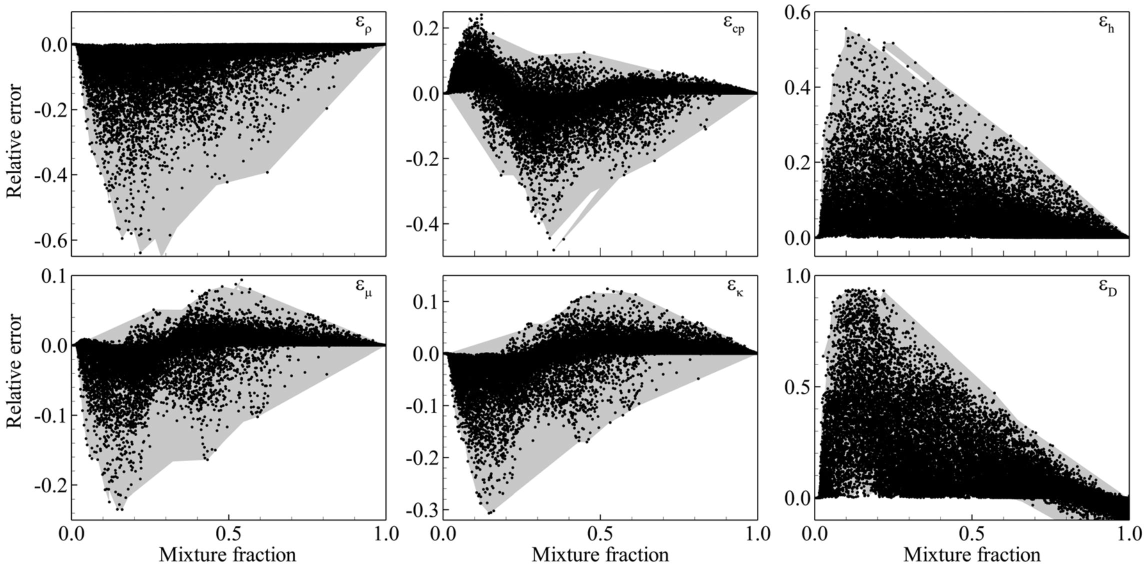

FIG. 8. Relative errors in filtered property calculations as a function of mixture fraction. $\varepsilon_\phi = (\overline{\phi(\mathbf{Q})} - \phi(\widetilde{\mathbf{Q}})/\overline{\phi(\mathbf{Q})})$. (Top) density, specific heat capacity, and specific enthalpy, (bottom) dynamic viscosity, thermal conductivity, and mass diffusivity of methane, $\overline{\Delta} = 20\Delta_{DNS}$ (nonreacting).

assessment of the exact terms in the filtered governing equations as derived from Sec. II B.

3. Order of magnitude analysis of terms in the governing LES equations for the nonreacting case

The results in Sec. IV A 2 clearly demonstrate that there are notable differences between the exact filtered and LES approximated quantities. However, the governing systems of equations comprised of derivatives of these terms coupled with other flow quantities. A detailed order of magnitude analysis is required to determine the extent to which these differences manifest within the terms in the governing equations in comparison to the leading order resolved terms, and how they affect the overall accuracy and fidelity of the numerical approach. This would help identify the terms that are most important to consider for LES modeling. To quantify the magnitude of each term in the LES equations, the rms for each term ψ is calculated as

$$\psi_{RMS} = \sqrt{\frac{1}{N}\left(\sum_{i=1}^{N}\left(\psi^i\right)^2\right)}, \tag{41}$$

where N is the total number of numerical cells used for calculating the statistics, and ψ^i is the value of the term for cell i. Only cells in the core of the mixing layer are used to compute the rms. The computed values have been verified to provide a reasonable estimate of the order of magnitude of the corresponding terms in the core of the mixing layer. A similar methodology was employed by Selle *et al.*[28] to assess the terms in the filtered equations.

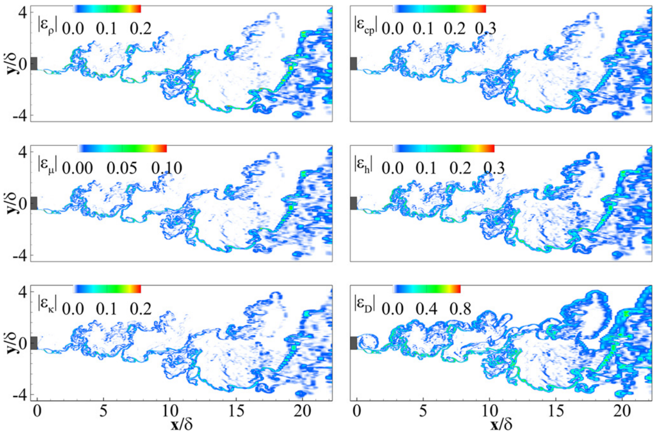

FIG. 9. Spatial distributions of error in calculation of filtered properties, $\overline{\Delta} = 10\Delta_{DNS}$ (nonreacting).

The exact value of each term in Eqs. (23)–(26) is evaluated using the DNS dataset and the rms of these terms are shown in Table I. The convective flux terms and the associated subgrid fluxes are the leading terms in all the governing equations, which is expected in high Reynolds number flows. In addition, we find that the derivatives of terms containing the subgrid density ρ^{sgs}, i.e., $\rho^{sgs}\widetilde{u}_i$, $\rho^{sgs}\widetilde{u}_i\widetilde{u}_j$, $\rho^{sgs}\widetilde{u}_i\widetilde{Y}_j$, and $(\rho H)^{sgs}$ are just one order of magnitude smaller than the leading convective terms, and comparable to the traditional SGS convective flux terms. In fact, the magnitude of terms involving subgrid density is sometimes higher than that of the conventional SGS terms. For example, in the u-momentum equation, the rms of the $\rho^{sgs}\widetilde{u}_i\widetilde{u}_j$ term is 7% of the corresponding convection term, and an order of magnitude larger than the traditional SGS stress term τ_{xx}^{sgs}. Although the error in property calculation for the filtered density is mostly within 20%, the flux associated with the corresponding terms is significant. Therefore, the modeling errors resulting from the evaluation of filtered density need to be accounted for.

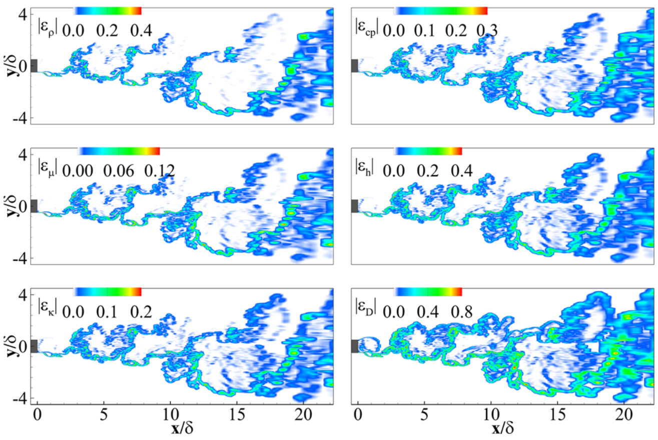

FIG. 10. Spatial distributions of error in calculation of filtered properties, $\overline{\Delta} = 20\Delta_{DNS}$ (nonreacting).

The viscous and diffusion terms are approximately 3–4 orders of magnitude smaller than the convective flux terms in accordance with the high Reynolds number. The subgrid quantities associated with these terms in Eqs. (20)–(22), however, are of the same order of magnitude as the corresponding diffusive flux terms. While these terms are much smaller in magnitude compared to the leading terms in the governing equations, they still need to be considered to accurately model the molecular diffusive processes which play an important role in the dissipation of energy at the smallest scales.

The third row in the tables present the corresponding rms values of the terms for the coarser filter size, $\overline{\Delta} = 20\Delta_{\mathrm{DNS}}$. The gradients of the resolved flow quantities are slightly diminished with a coarser grid resolution, as more small-scale fluctuations are filtered out. This trend is seen primarily for all the leading order resolved terms in the governing equations. With increase in filter size, the amount of content at the subgrid level increases, and the magnitude of the subgrid fluxes is consequently higher. The corresponding derivative terms in the governing equations increase slightly or remain about the same due to a combined effect of increase in magnitude of the subgrid term itself and a decrease due to increase in filter size (decrease in spatial derivative). As result, the subgrid terms retain their order of magnitude with respect to the fine filter size. However, their magnitude becomes more significant with respect to the leading resolved terms. For example, in the u-momentum equation, the relative magnitude of $\rho^{sgs}\widetilde{u}_i\widetilde{u}_j$ increases from 7% to 13.5% with respect to the resolved convective flux term $\rho\big(\widetilde{\mathbf{Q}}\big)\widetilde{u}\widetilde{u}$, while τ_{xx}^{sgs} is also nearly doubled. The same trend is also observed with corresponding terms in the other governing equations. The subgrid terms associated with the diffusive (viscous) flux terms decrease slightly but still remain comparable in order of magnitude with respect to their corresponding resolved flux terms. Thus, the issues with unclosed subgrid terms, particularly those associated with the subgrid density, can be significant with respect to the governing equations and play an important role in determining the flow evolution and prediction of turbulent mixing characteristics. The relevance of these terms increases with filter size, which poses an important consideration for coarse LES simulations.

B. Reacting flow (supercritical turbulent combustion)

In this section, we investigate the subgrid modeling issues highlighted earlier in the context of multispecies reacting flows at the same operating conditions.

1. Instantaneous reacting flowfield

Figure 11 shows the instantaneous distributions of density, temperature, and OH species mass fraction, along with a simulated shadowgraph visualization, for the combustion case. Fine-scale structures of the turbulent flowfield and its interaction with the flame structure are observable in the DNS results. The flame is anchored in the recirculation zone immediately downstream of the splitter plate. It then spreads as the vortices roll up and develop downstream. The predicted scalar dissipation rate in the near field of the splitter plate is too small to quench the flamelets, so the flame is stabilized at the LOX post. Since the flame is mixing- and diffusion-controlled, the flame structure correlates strongly with the mixing layers. The combustion process introduces very large temperature gradients, which in turn induce rapid thermodynamic variations in the flame zone. The distributions of species mass fractions and density show that the shedding of unburned liquid oxygen from the liquid oxygen stream due to the shear stress from the hot combustion products results in broad expansion of the flame. The unburned oxygen ligaments continue to mix with methane in the outer region and form a secondary flame, which persists for a short time before the oxygen parcels are completely depleted through reaction with rich mixtures. It then either merges with larger flame structures through vortex rolling/pairing or disappears by dilution into the low-temperature fuel stream. The secondary flame is also observed in Singla *et al.*,[7] but the mechanism is different. Here, the secondary flame is formed from large-scale mixing of fuel and oxidizer, whereas in Singla's experiments droplet penetration accounts for the secondary flame.

As the flame is convected downstream, multiple pairings of vortices change the flame structure to a big multifold plume. The small flame structures then mix with cold reactants and lose energy. The flame generally continues to follow the oxygen stream and remains close to the high-density oxygen. A small fraction of LOX is heated to form gaseous oxygen, which is sufficient to react with the methane brought up by turbulent mixing.

2. Modeling errors in computation of filtered flow properties

Figures 12 and 13 present the relative errors in calculating $\overline{\phi(\mathbf{Q})}$ as $\phi\big(\widetilde{\mathbf{Q}}\big)$ for density, specific heat at constant pressure, specific enthalpy, dynamic viscosity, thermal conductivity, and mass diffusivity of methane at a filter size of $\overline{\Delta} = 10\Delta_{DNS}$ and $\overline{\Delta} = 20\Delta_{DNS}$, respectively. The distributions of the errors are more complex than their counterpart in the nonreacting flow. First, the errors in most properties are significantly larger than those observed for the nonreacting case, especially for the specific heat, molecular viscosity, and thermal conductivity. Second, the errors are spread over a wider region in the mixture fraction space.

In the nonreacting flow, the variation of temperature and species mass fraction is much smaller. The release of chemical potential

TABLE I. Significance of each term in the LES governing equations (nonreacting case), (row 2: $\overline{\Delta} = 10\Delta_{DNS}$, row 3: $\overline{\Delta} = 20\Delta_{DNS}$).

a. RMS of each term in the continuity equation, unit: $10^8\ \mathrm{kg\,m^{-3}\,s^{-1}}$

$\frac{\partial \rho(\widetilde{Q})\widetilde{u}}{\partial x}$	$\frac{\partial \rho(\widetilde{Q})\widetilde{v}}{\partial y}$	$\frac{\partial(\rho^{sgs}\widetilde{u})}{\partial x}$	$\frac{\partial(\rho^{sgs}\widetilde{v})}{\partial y}$
1.0	0.9	9.0×10^{-2}	1.4×10^{-1}
0.6	0.6	9.7×10^{-2}	1.4×10^{-1}

b. RMS of each term in the x-momentum equation, unit: $10^8\ \mathrm{kg\,m^{-2}\,s^{-2}}$

$\frac{\partial \rho(\widetilde{Q})\widetilde{u}\widetilde{u}}{\partial x}$	$\frac{\partial \rho(\widetilde{Q})\widetilde{u}\widetilde{v}}{\partial y}$	$\frac{\partial \tau_{xx}(\widetilde{Q})}{\partial x}$	$\frac{\partial \tau_{xy}(\widetilde{Q})}{\partial y}$	$\frac{\partial \overline{p}}{\partial x}$
40.1	20.2	3.2×10^{-3}	2.7×10^{-2}	3.5
23.0	13.6	1.3×10^{-3}	1.5×10^{-2}	3.0

$\frac{\partial \rho^{sgs}\widetilde{u}\widetilde{u}}{\partial x}$	$\frac{\partial \rho^{sgs}\widetilde{u}\widetilde{v}}{\partial y}$	$\frac{\partial \Delta\tau_{xx}}{\partial x}$	$\frac{\partial \Delta\tau_{xy}}{\partial y}$	$\frac{\partial \tau_{xx}^{sgs}}{\partial x}$	$\frac{\partial \tau_{xy}^{sgs}}{\partial y}$
2.8	2.2	1.3×10^{-3}	9.3×10^{-3}	0.2	0.6
3.1	2.4	7.7×10^{-4}	5.1×10^{-3}	0.2	0.7

c. RMS of each term in the y-momentum equation, unit: $10^8\ \mathrm{kg\,m^{-2}\,s^{-2}}$

$\frac{\partial \rho(\widetilde{Q})\widetilde{u}\widetilde{v}}{\partial x}$	$\frac{\partial \rho(\widetilde{Q})\widetilde{v}\widetilde{v}}{\partial y}$	$\frac{\partial \tau_{yx}(\widetilde{Q})}{\partial x}$	$\frac{\partial \tau_{yy}(\widetilde{Q})}{\partial y}$	$\frac{\partial \overline{p}}{\partial y}$
12.1	13.2	4.0×10^{-3}	1.1×10^{-2}	3.6
7.6	8.6	1.9×10^{-3}	5.6×10^{-3}	3.3

$\frac{\partial \rho^{sgs}\widetilde{v}\widetilde{u}}{\partial x}$	$\frac{\partial \rho^{sgs}\widetilde{v}\widetilde{v}}{\partial y}$	$\frac{\partial \Delta\tau_{yx}}{\partial x}$	$\frac{\partial \Delta\tau_{yy}}{\partial y}$	$\frac{\partial \tau_{yx}^{sgs}}{\partial x}$	$\frac{\partial \tau_{yy}^{sgs}}{\partial y}$
0.8	1.6	2.2×10^{-3}	6.5×10^{-3}	0.2	0.6
0.8	1.6	1.2×10^{-3}	3.4×10^{-3}	0.2	0.9

d. RMS of each term in the energy equation, unit: $10^{12}\ \mathrm{kg\,m^{-1}\,s^{-3}}$

$\frac{\partial \rho(\widetilde{Q})H(\widetilde{Q})\widetilde{u}}{\partial x}$	$\frac{\partial \rho(\widetilde{Q})H(\widetilde{Q})\widetilde{v}}{\partial y}$	$\frac{\partial \sigma_x^{sgs}}{\partial x}$	$\frac{\partial \sigma_y^{sgs}}{\partial y}$	$\frac{\partial \tau_{xj}(\widetilde{Q})\widetilde{u}_j}{\partial x}$	$\frac{\partial \tau_{yj}(\widetilde{Q})\widetilde{u}_j}{\partial y}$	$\frac{\partial q_x(\widetilde{Q})}{\partial x}$	$\frac{\partial q_y(\widetilde{Q})}{\partial y}$
73.0	78.1	2.7×10^{-6}	1.0×10^{-5}	9.8×10^{-6}	8.0×10^{-5}	3.5×10^{-3}	5.4×10^{-2}
50.1	59.4	1.9×10^{-6}	5.4×10^{-6}	3.8×10^{-6}	3.8×10^{-5}	1.2×10^{-3}	2.2×10^{-2}

$\frac{\partial(\rho H)^{sgs}\widetilde{u}}{\partial x}$	$\frac{\partial(\rho H)^{sgs}\widetilde{v}}{\partial y}$	$\frac{\partial H_x^{sgs}}{\partial x}$	$\frac{\partial H_y^{sgs}}{\partial y}$	$\frac{\partial \Delta\tau_{xj}\widetilde{u}_j}{\partial x}$	$\frac{\partial \Delta\tau_{yj}\widetilde{u}_j}{\partial y}$	$\frac{\partial q_x^{sgs}}{\partial x}$	$\frac{\partial q_y^{sgs}}{\partial y}$
11.7	18.8	22.8	33.6	4.9×10^{-6}	3.0×10^{-5}	2.3×10^{-3}	2.6×10^{-2}
12.4	18.5	25.3	32.7	2.4×10^{-6}	1.5×10^{-5}	9.4×10^{-4}	1.4×10^{-3}

e. RMS of each term in the CH_4 mass fraction equation, unit: $10^7\ \mathrm{kg\,m^{-3}\,s^{-1}}$

$\frac{\partial \rho(\widetilde{Q})\widetilde{u}\widetilde{Y}_{CH4}}{\partial x}$	$\frac{\partial \rho(\widetilde{Q})\widetilde{v}\widetilde{Y}_{CH4}}{\partial y}$	$\frac{\partial j_{x,CH4}}{\partial x}$	$\frac{\partial j_{y,CH4}}{\partial y}$
1.4	1.6	8.1×10^{-4}	1.4×10^{-2}
0.9	1.2	2.6×10^{-4}	5.6×10^{-3}

$\frac{\partial \rho^{sgs}\widetilde{u}\widetilde{Y}_{CH4}}{\partial x}$	$\frac{\partial \rho^{sgs}\widetilde{v}\widetilde{Y}_{CH4}}{\partial y}$	$\frac{\partial \Delta j_{x,CH4}}{\partial x}$	$\frac{\partial \Delta j_{y,CH4}}{\partial y}$	$\frac{\partial \phi_{x,CH4}^{sgs}}{\partial x}$	$\frac{\partial \phi_{y,CH4}^{sgs}}{\partial y}$
0.2	0.3	7.0×10^{-4}	8.9×10^{-3}	0.2	0.3
0.2	0.3	2.8×10^{-4}	4.4×10^{-3}	0.2	0.3

energy in the combustion case broadens the range of variation of temperature in addition to rapid variations of species concentrations. The thermodynamic and transport properties are a function of temperature and species concentrations, and this dependence becomes more complex and nonlinear for multispecies reacting flows due to the mixing laws.[16] The SGS fluctuations of these variables thus contribute to the uncertainty of filtered flow properties. The first moments of the independent state variables cannot uniquely and accurately represent the thermodynamic status of the fluid parcel enclosed by the LES filter, and this results in substantial deviation of $\phi(\widetilde{\mathbf{Q}})$ from $\overline{\phi(\mathbf{Q})}$.

The mixture composition and temperature vary rapidly in the flowfield, due to the flow turbulence and flame structures. Each of the species components have a unique thermodynamic behavior, which in turn alter the thermodynamic properties of the resulting mixture depending upon the instantaneous species composition through the nonlinear mixing laws. The critical points of the mixture could be significantly different from that of the constituent species, and the mixture could undergo transition from ideal gas to supercritical fluid phase and vice versa in the flame regions. This gives rise to significant variation of the thermodynamic and transport properties at various

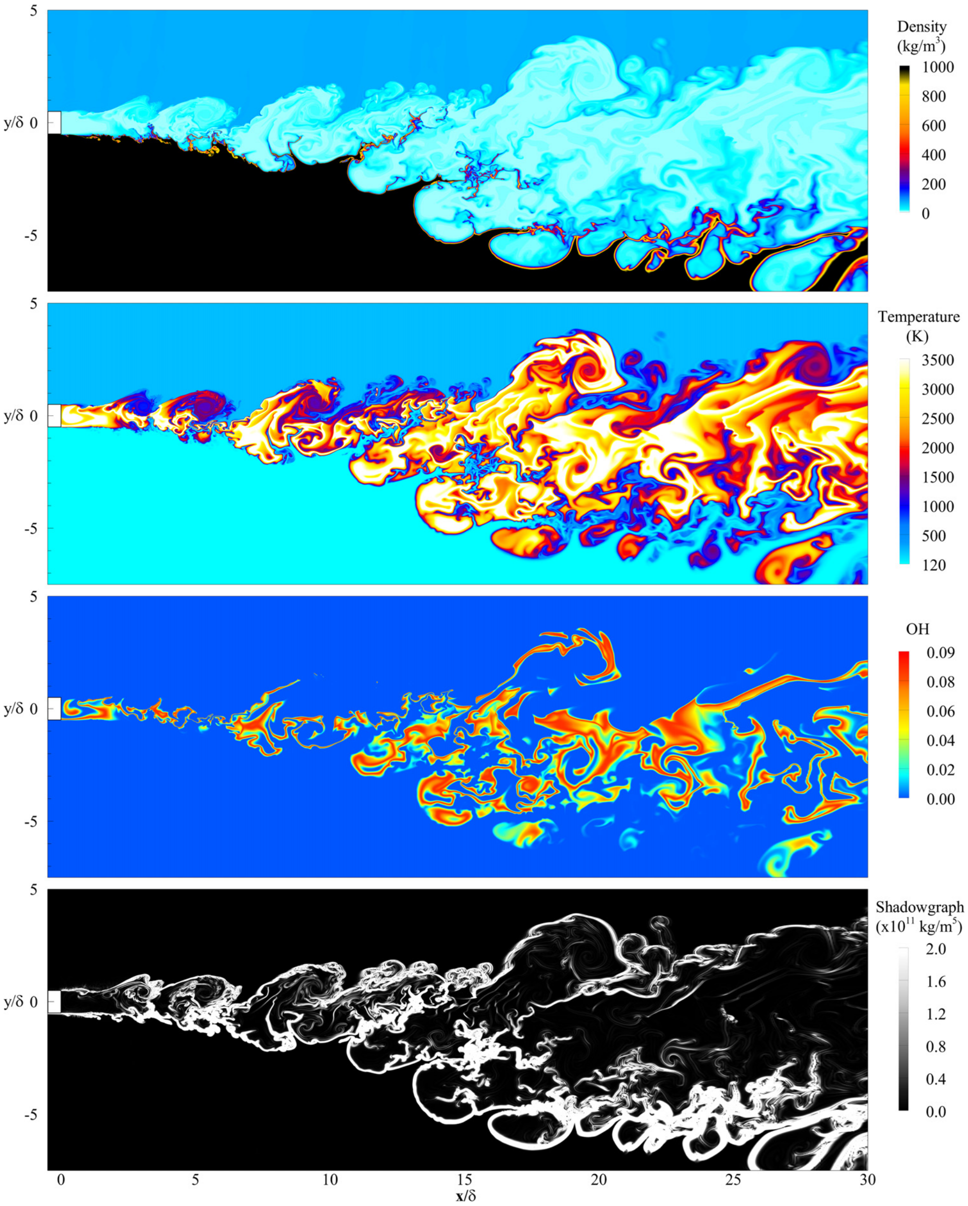

FIG. 11. Instantaneous visualizations of reacting flowfield: distributions of density, temperature and OH mass fraction, and shadowgraph visualization (from top to bottom).

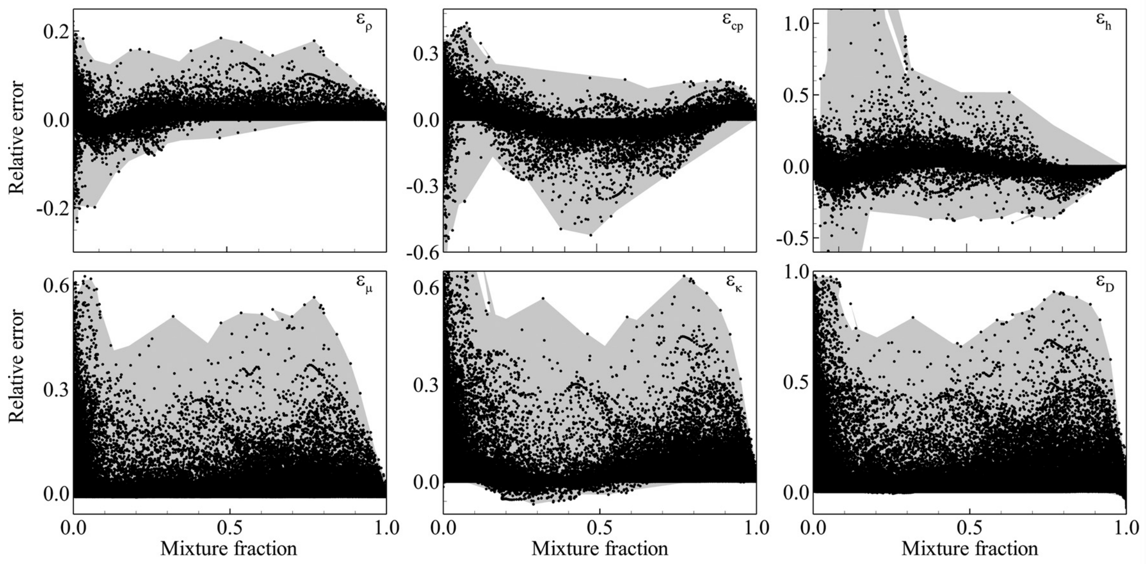

FIG. 12. Relative errors in filtered property calculations as a function of mixture fraction. $\varepsilon_\phi = (\overline{\phi(\mathbf{Q})} - \phi(\widetilde{\mathbf{Q}}))/\overline{\phi(\mathbf{Q})}$, $\overline{\Delta} = 10\Delta_{DNS}$ (reacting).

length scales. The LES filtering procedure of these turbulence-chemistry interactions results in complex behavior of the errors in the calculation of filtered mixture properties. This reinforces the impact of the nonlinear nature of the thermodynamic and transport property calculations for LES of multicomponent real-fluid mixtures.

The distributions of the error magnitudes in the calculated filtered properties for the two filter sizes are shown in Figs. 14 and 15, respectively. In contrast to the nonreacting case, where the error distribution was largely across the transcritical mixing layer close to the oxygen stream, the peak errors in the reacting case occur in two branches—one corresponding to the stoichiometric flame surface that occurs closer to the oxygen stream, and the other closer to the methane stream at the interface between the methane stream and hot flame products. The error in the filtered density is smaller compared to the nonreacting case. This may be attributed to the fact that the compressibility factor Z of the hot gases in the flame and combustion products

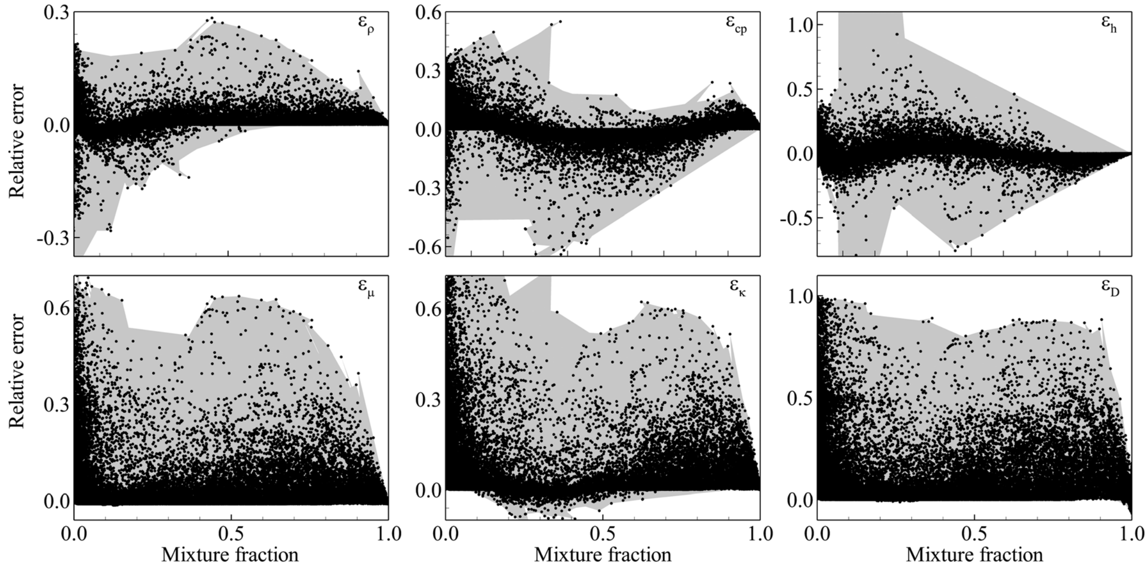

FIG. 13. Relative errors in filtered property calculations as a function of mixture fraction. $\varepsilon_\phi = (\overline{\phi(\mathbf{Q})} - \phi(\widetilde{\mathbf{Q}}))/\overline{\phi(\mathbf{Q})}$, $\overline{\Delta} = 20\Delta_{DNS}$ (reacting).

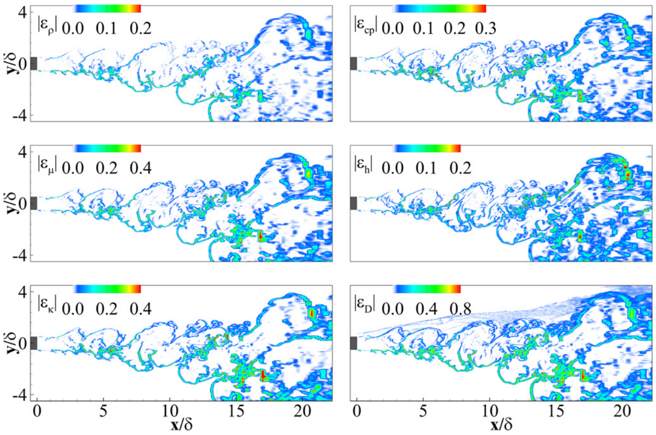

FIG. 14. Spatial distributions of error in the calculation of filtered properties, $\overline{\Delta} = 10\Delta_{DNS}$ (reacting).

is close to one, thereby minimizing the effect of subgrid fluctuations of Z on the filtered density. An error still persists due to the subgrid fluctuations in temperature and species mass fractions, pointing to the fact that their SGS effects are also relevant for ideal, multicomponent flows. The effect of these errors has to be evaluated in light of their contribution through their counterpart terms in the governing equations. This will be discussed in Sec. IV B 3. Similar to the nonreacting case, the overall error in filtered property calculations increases with increasing filter size, along with a slight increase in the maximum error as seen in Fig. 13.

3. Order of magnitude analysis of terms in the governing LES equations for the reacting case

Following the same procedure as Sec. IV A 3, the terms in the governing filtered equations are calculated for the reacting flow case. Table II shows the rms values of each term in the filtered equations for the two filter widths. Similar to the nonreacting flow case, the convective terms, along with the corresponding traditional SGS flux terms, are among the leading terms in all of the governing equations. It is noted that the Reynolds number is smaller in the combustion case, because density is reduced and viscosity is larger in the flame zone due to increased temperature. The magnitudes of the molecular diffusion terms (relative to the convective terms) are higher compared to the nonreacting case, but still about two to three orders of magnitude smaller than the convection terms and the SGS flux terms.

Table II strongly indicates the importance of correctly modeling subgrid density ρ^{sgs} and $(\rho H)^{sgs}$. The magnitudes of these terms are significantly increased and these are almost of same magnitude as the resolved convective flux terms and higher than the SGS convective fluxes. The SGS convective fluxes are more relevant in the energy and species conservation equations and are diminished in the momentum equations. The subgrid terms associated with the diffusive flux terms are still comparable in magnitude to the corresponding resolved terms

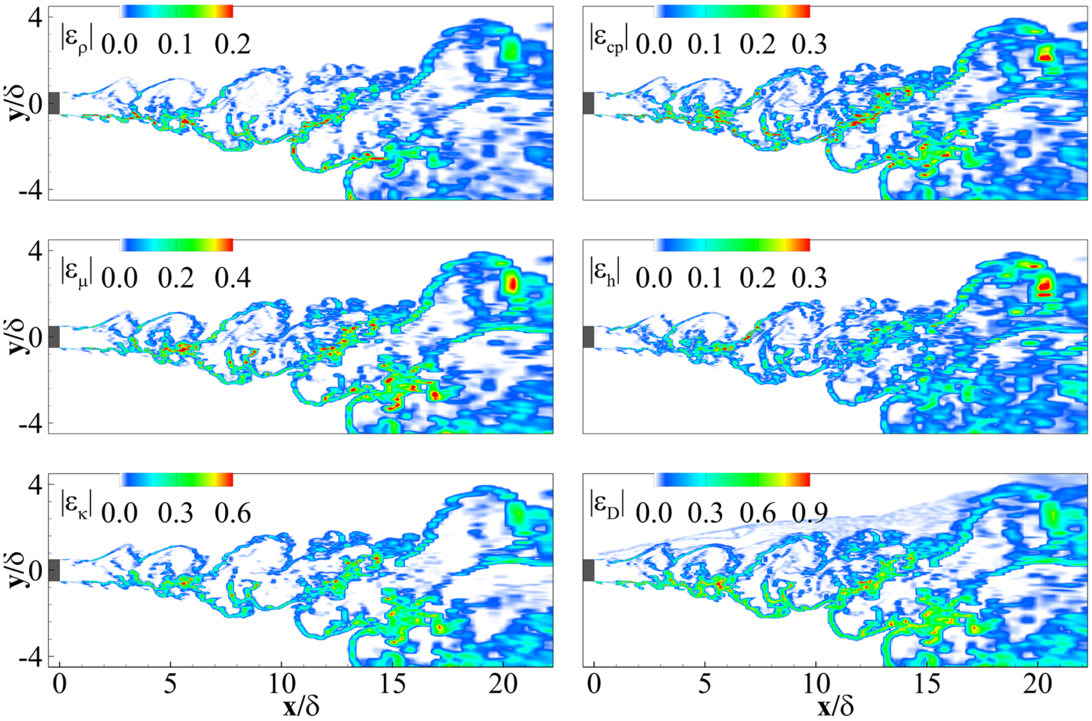

FIG. 15. Spatial distributions of error in the calculation of filtered properties, $\overline{\Delta} = 20\Delta_{DNS}$ (reacting).

TABLE II. Significance of each term in the LES governing equations (reacting case), row 2: $\overline{\Delta} = 10\Delta_{\mathrm{DNS}}$, row 3: $\overline{\Delta} = 20\Delta_{\mathrm{DNS}}$.

a. RMS of each term in the continuity equation, unit: $10^7\ \mathrm{kg\,m^{-3}\,s^{-1}}$

$\frac{\partial \rho(\widetilde{Q})\widetilde{u}}{\partial x}$	$\frac{\partial \rho(\widetilde{Q})\widetilde{v}}{\partial y}$	$\frac{\partial(\rho^{sgs}\widetilde{u})}{\partial x}$	$\frac{\partial(\rho^{sgs}\widetilde{v})}{\partial y}$
5.2	4.3	0.7	0.5
3.1	2.8	0.6	0.4

b. RMS of each term in the x-momentum equation, unit: $10^8\ \mathrm{kg\,m^{-2}\,s^{-2}}$

$\frac{\partial \rho(\widetilde{Q})\widetilde{u}\widetilde{u}}{\partial x}$	$\frac{\partial \rho(\widetilde{Q})\widetilde{u}\widetilde{v}}{\partial y}$	$\frac{\partial \tau_{xx}(\widetilde{Q})}{\partial x}$	$\frac{\partial \tau_{xy}(\widetilde{Q})}{\partial y}$	$\frac{\partial \overline{p}}{\partial x}$	
11.5	7.9	8.9×10^{-3}	4.0×10^{-2}	9.8	
6.7	5.4	4.0×10^{-3}	2.0×10^{-2}	5.8	
$\frac{\partial \rho^{sgs}\widetilde{u}\widetilde{u}}{\partial x}$	$\frac{\partial \rho^{sgs}\widetilde{u}\widetilde{v}}{\partial y}$	$\frac{\partial \Delta\tau_{xx}}{\partial x}$	$\frac{\partial \Delta\tau_{xy}}{\partial y}$	$\frac{\partial \tau_{xy}^{sgs}}{\partial x}$	$\frac{\partial \tau_{xy}^{sgs}}{\partial y}$
1.2	0.7	5.6×10^{-3}	2.2×10^{-2}	4.7×10^{-2}	1.6×10^{-1}
0.9	0.5	3.0×10^{-3}	1.5×10^{-2}	5.4×10^{-2}	2.2×10^{-1}

c. RMS of each term in the y-momentum equation, unit: $10^8\ \mathrm{kg\,m^{-2}\,s^{-2}}$

$\frac{\partial \rho(\widetilde{Q})\widetilde{u}\widetilde{v}}{\partial x}$	$\frac{\partial \rho(\widetilde{Q})\widetilde{v}\widetilde{v}}{\partial y}$	$\frac{\partial \tau_{yx}(\widetilde{Q})}{\partial x}$	$\frac{\partial \tau_{yy}(\widetilde{Q})}{\partial y}$	$\frac{\partial \overline{p}}{\partial y}$	
2.6	2.2	1.0×10^{-2}	7.4×10^{-2}	57.1	
1.7	1.5	3.7×10^{-3}	5.2×10^{-2}	40.6	
$\frac{\partial \rho^{sgs}\widetilde{v}\widetilde{u}}{\partial x}$	$\frac{\partial \rho^{sgs}\widetilde{v}\widetilde{v}}{\partial y}$	$\frac{\partial \Delta\tau_{yx}}{\partial x}$	$\frac{\partial \Delta\tau_{yy}}{\partial y}$	$\frac{\partial \tau_{yx}^{sgs}}{\partial x}$	$\frac{\partial \tau_{yy}^{sgs}}{\partial y}$
0.2	0.2	4.4×10^{-3}	1.8×10^{-2}	3.7×10^{-2}	2.9×10^{-1}
0.14	0.14	2.6×10^{-3}	1.4×10^{-2}	4.4×10^{-2}	3.6×10^{-1}

d. RMS of each term in the energy equation, unit: $10^{12}\ \mathrm{kg\,m^{-1}\,s^{-3}}$

$\frac{\partial \rho(\widetilde{Q})H(\widetilde{Q})\widetilde{u}}{\partial x}$	$\frac{\partial \rho(\widetilde{Q})H(\widetilde{Q})\widetilde{v}}{\partial y}$	$\frac{\partial \sigma_x^{sgs}}{\partial x}$	$\frac{\partial \sigma_y^{sgs}}{\partial y}$	$\frac{\partial \tau_{xj}(\widetilde{Q})\widetilde{u}_j}{\partial x}$	$\frac{\partial \tau_{yj}(\widetilde{Q})\widetilde{u}_j}{\partial y}$	$\frac{\partial q_x(\widetilde{Q})}{\partial x}$	$\frac{\partial q_y(\widetilde{Q})}{\partial y}$
67.5	68.3	3.5×10^{-6}	2.5×10^{-5}	3.1×10^{-5}	1.7×10^{-4}	2.6×10^{-1}	2.3
44.3	49.0	2.3×10^{-6}	1.7×10^{-5}	1.3×10^{-5}	8.5×10^{-5}	9.2×10^{-2}	1.0
$\frac{\partial(\rho H)^{sgs}\widetilde{u}}{\partial x}$	$\frac{\partial(\rho H)^{sgs}\widetilde{v}}{\partial y}$	$\frac{\partial H_x^{sgs}}{\partial x}$	$\frac{\partial H_y^{sgs}}{\partial y}$	$\frac{\partial \Delta\tau_{xj}\widetilde{u}_j}{\partial x}$	$\frac{\partial \Delta\tau_{yj}\widetilde{u}_j}{\partial y}$	$\frac{\partial q_x^{sgs}}{\partial x}$	$\frac{\partial q_y^{sgs}}{\partial y}$
3.6	3.0	2.7	2.6	2.0×10^{-5}	7.2×10^{-5}	2.2×10^{-1}	1.4
3.0	2.5	2.6	2.5	1.0×10^{-5}	4.5×10^{-5}	9.4×10^{-2}	0.7

e. RMS of each term in the CH_4 mass fraction equation, unit: $10^7\ \mathrm{kg\,m^{-3}\,s^{-1}}$

$\frac{\partial \rho^{sgs}\widetilde{u}\widetilde{Y}_{CH4}}{\partial x}$	$\frac{\partial \rho^{sgs}\widetilde{v}\widetilde{Y}_{CH4}}{\partial y}$	$\frac{\partial \Delta j_{CH4,x}}{\partial x}$	$\frac{\partial \Delta j_{CH4,y}}{\partial y}$		
1.4	1.4	1.6×10^{-3}	1.6×10^{-2}		
0.9	1.0	5.9×10^{-4}	7.6×10^{-3}		
$\frac{\partial \rho^{sgs}\widetilde{u}\widetilde{Y}_{CH4}}{\partial x}$	$\frac{\partial \rho^{sgs}\widetilde{v}\widetilde{Y}_{CH4}}{\partial y}$	$\frac{\partial \Delta j_{CH4,x}}{\partial x}$	$\frac{\partial \Delta j_{CH4,y}}{\partial y}$	$\frac{\partial \phi_{CH4,x}^{sgs}}{\partial x}$	$\frac{\partial \phi_{CH4,y}^{sgs}}{\partial y}$
3.2×10^{-2}	2.7×10^{-2}	1.2×10^{-3}	1.2×10^{-2}	3.1×10^{-2}	3.4×10^{-2}
3.1×10^{-2}	2.5×10^{-2}	5.1×10^{-4}	5.6×10^{-3}	3.0×10^{-2}	3.4×10^{-2}

computed from filtered flow variables. The relevance of modeling these terms requires further investigation.

The trends with an increase in filter size are similar to those observed for the nonreacting case. The magnitude of terms associated with the resolved flow quantities decreases, while those associated with the subgrid terms remain about the same with a marginal decrease. Therefore, the subgrid terms are expected to become more significant with respect to the resolved terms as the filter size increases. Accurate modeling of subgrid terms is imperative for coarse LES simulations.

V. CONCLUSIONS AND FUTURE WORK

The present work highlights important subgrid modeling issues for accurate LES simulations of transcritical and supercritical mixing and combustion. We revisited the LES governing equations with the retention of all the associated SGS terms, and investigated these terms in light of two-dimensional DNS of transcritical mixing layers at operating conditions representative of fluid injection, mixing, and combustion in practical combustion systems.

The underlying modeling assumptions and subgrid effects associated with the computation of secondary variables in the LES formulation, which are neglected in the conventional framework and implementations, were reexamined. While these simplifications might be valid for ideal, single-component gas flows, their extension to supercritical, multicomponent mixtures is questionable. We investigated these assumptions by accounting all the subgrid terms that arise from the filtering operation, and evaluating the order of magnitude of these terms with respect to the leading physical terms in the governing equations. It was found that some of these terms, including those associated with the direct evaluation of filtered thermodynamic and transport properties, are substantial in magnitude and hence should be considered in the modeling process. The subgrid density arising from the filtering of the real-fluid equation of state is especially important, due to its presence in all the governing equations and the magnitude of the resulting terms. There are also subgrid terms associated with filtering the diffusive fluxes. While these terms are much smaller in magnitude with respect to the resolved convective terms, they are still comparable in magnitude to the resolved diffusive fluxes and play an important role in the dissipation and diffusion processes at the small scales. These terms require further investigation and modeling efforts.

The issues presented in this work are especially important for transcritical and supercritical fluid flows and combustion, involving real-fluid transport, multispecies mixing and reacting flows at supercritical pressures, where the mixture properties are highly nonlinear functions of the species composition and thermodynamic state. Accurate modeling of subgrid turbulence-chemistry interactions and its effect on real-fluid thermodynamics and transport is principal to ensure a consistent and accurate LES formulation. The increase in relevance of subgrid terms with an increase in filter size presents an important consideration for LES and RANS applications for complex systems, where an appropriate grid resolution is essential to balance the computational cost and accuracy.

Future work will focus on assessing the accuracy of current SGS models under supercritical conditions and explore modeling approaches for the new set of subgrid terms identified in this paper. The important considerations highlighted in this work warrant detailed investigation under a wide range of flow conditions using data from three-dimensional DNS simulations, when such studies are feasible.

ACKNOWLEDGMENTS

This work was supported partly by the Air Force Office of Scientific Research (AFOSR) under Grant No. FA9550-18-1-0216, and partly by the William R. T. Oakes Endowment and the Ralph N. Read Endowment of the Georgia Institute of Technology. The authors gratefully acknowledge support and advice from Mitat A. Birkan.

DATA AVAILABILITY

The data that support the findings of this study are available from the corresponding author upon reasonable request.

REFERENCES

[1] V. Yang, "Modeling of supercritical vaporization, mixing, and combustion processes in liquid-fueled propulsion systems," Proc. Combust. Inst. **28**, 925 (2000).

[2] J. Bellan, "Supercritical (and subcritical) fluid behavior and modeling: Drops, streams, shear and mixing layers, jets and sprays," Prog. Energy Combust. Sci. **26**, 329 (2000).

[3] R. N. Dahms and J. C. Oefelein, "On the transition between two-phase and single-phase interface dynamics in multicomponent fluids at supercritical pressures," Phys. Fluids **25**, 092103 (2013).

[4] W. Mayer and H. Tamura, "Propellant injection in a liquid oxygen/gaseous hydrogen rocket engine," J. Propul. Power **12**, 1137 (1996).

[5] W. Mayer, A. Schik, M. Schaffler, and H. Tamura, "Injection and mixing processes in high-pressure liquid oxygen/gaseous hydrogen rocket combustors," J. Propul. Power **16**, 823 (2000).

[6] B. Chehroudi, D. Talley, and E. Coy, "Visual characteristics and initial growth rates of round cryogenic jets at subcritical and supercritical pressures," Phys. Fluids **14**, 850 (2002).

[7] G. Singla, P. Scouflaire, C. Rolon, and S. Candel, "Transcritical oxygen/transcritical or supercritical methane combustion," Proc. Combust. Inst. **30**, 2921 (2005).

[8] C. Segal and S. Polikhov, "Subcritical to supercritical mixing," Phys. Fluids **20**, 052101 (2008).

[9] A. Roy and C. Segal, "Experimental study of fluid jet mixing at supercritical conditions," J. Propul. Power **26**, 1205 (2010).

[10] J. C. Oefelein and V. Yang, "Modeling high-pressure mixing and combustion processes in liquid rocket engines," J. Propul. Power **14**, 843 (1998).

[11] R. N. Dahms and J. C. Oefelein, "Liquid jet breakup regimes at supercritical pressures," Combust. Flame **162**, 3648 (2015).

[12] J. Poblador-Ibanez and W. A. Sirignano, "Transient behavior near liquid–gas interface at supercritical pressure," Int. J. Heat Mass Transfer **126**, 457 (2018).

[13] L. Jofre and J. Urzay, "Transcritical diffuse-interface hydrodynamics of propellants in high-pressure combustors of chemical propulsion systems," Prog. Energy Combust. Sci. **82**, 100877 (2021).

[14] H. Meng and V. Yang, "A unified treatment of general fluid thermodynamics and its application to a preconditioning scheme," J. Comput. Phys. **189**, 277 (2003).

[15] F. Ries and A. Sadiki, "Supercritical and transcritical turbulent injection processes: Consistency of numerical modeling," Atomization Sprays **31**, 37 (2021).

[16] V. Giovangigli and L. Matuszewski, "Mathematical modeling of supercritical multicomponent reactive fluids," Math. Models Methods Appl. Sci. **23**, 2193 (2013).

[17] P. C. Ma, H. Wu, D. T. Banuti, and M. Ihme, "On the numerical behavior of diffuse-interface methods for transcritical real-fluids simulations," Int. J. Multiphase Flow **113**, 231 (2019).

[18] T. Schmitt, Y. Méry, M. Boileau, and S. Candel, "Large-eddy simulation of oxygen/methane flames under transcritical conditions," Proc. Combust. Inst. **33**, 1383 (2011).

[19] X. Petit, G. Ribert, G. Lartigue, and P. Domingo, "Large-eddy simulation of supercritical fluid injection," J. Supercrit. Fluids **84**, 61 (2013).

[20]J. Bellan, *High-Pressure Flows for Propulsion Applications* (American Institute of Aeronautics and Astronautics, Inc., 2020).

[21]C. Meneveau and J. Katz, "Scale-invariance and turbulence models for large-eddy simulation," Annu. Rev. Fluid Mech. **32**, 1 (2000).

[22]J. Smagorinsky, "General circulation experiments with the primitive equations: I. The basic experiment," Mon. Weather Rev. **91**, 99 (1963).

[23]K. Lilly, "The representation of small-scale turbulence in numerical simulation experiments," *Proceedings of IBM Scientific Computing Symposium on Environmental Sciences* (IBM, White Plains, NY, 1967), p. 195.

[24]M. Germano, U. Piomelli, P. Moin, and W. H. Cabot, "A dynamic subgrid-scale eddy viscosity model," Phys. Fluids A **3**, 1760 (1991).

[25]D. K. Lilly, "A proposed modification of the Germano subgrid-scale closure method," Phys. Fluids A **4**, 633 (1992).

[26]J. Bardina, J. Ferziger, and, and W. Reynolds, "Improved subgrid-scale models for large-eddy simulation," in *AIAA 13th Fluid and Plasma Dynamics Conference* (AIAA, 1980), p. 1357.

[27]H. Müller, C. A. Niedermeier, J. Matheis, M. Pfitzner, and S. Hickel, "Large-eddy simulation of nitrogen injection at trans-and supercritical conditions," Phys. Fluids **28**, 015102 (2016).

[28]L. C. Selle, N. A. Okong'o, J. Bellan, and K. G. Harstad, "Modelling of subgrid-scale phenomena in supercritical transitional mixing layers: An *a priori* study," J. Fluid Mech. **593**, 57 (2007).

[29]M. Lee and R. D. Moser, "Direct numerical simulation of turbulent channel flow up to Re-tau approximate to 5200," J. Fluid Mech. **774**, 395 (2015).

[30]J. H. Chen, "Petascale direct numerical simulation of turbulent combustion—Fundamental insights towards predictive models," Proc. Combust. Inst. **33**, 99 (2011).

[31]J. Bellan, "Direct numerical simulation of a high-pressure turbulent reacting temporal mixing layer," Combust. Flame **176**, 245 (2017).

[32]G. Ribert, X. Petit, and P. Domingo, "High-pressure methane-oxygen flames. Analysis of sub-grid scale contributions in filtered equations of state," J. Supercrit. Fluids **121**, 78 (2017).

[33]P. E. Lapenna and F. Creta, "Mixing under transcritical conditions: An *a priori* study using direct numerical simulation," J. Supercrit. Fluids **128**, 263 (2017).

[34]P. Lapenna and F. Creta, "Direct numerical simulation of transcritical jets at moderate Reynolds number," AIAA J. **57**, 2254 (2019).

[35]J. C. Oefelein, "Thermophysical characteristics of shear-coaxial LOX–H_2 flames at supercritical pressure," Proc. Combust. Inst. **30**, 2929 (2005).

[36]J. C. Oefelein, "Mixing and combustion of cryogenic oxygen–hydrogen shear-coaxial jet flames at supercritical pressure," Combust. Sci. Technol. **178**, 229 (2006).

[37]A. M. Ruiz, G. Lacaze, J. C. Oefelein, R. l Mari, B. Cuenot, L. Selle, and T. Poinsot, "Numerical benchmark for high-Reynolds-number supercritical flows with large density gradients," AIAA J. **54**, 1445 (2016).

[38]N. A. Okong'o and J. Bellan, "Direct numerical simulation of a transitional supercritical binary mixing layer: Heptane and nitrogen," J. Fluid Mech. **464**, 1 (2002).

[39]J. F. Ely and H. Hanley, "Prediction of transport properties. 1. Viscosity of fluids and mixtures," Ind. Eng. Chem. Fundam. **20**, 323 (1981).

[40]J. F. Ely and H. Hanley, "Prediction of transport properties. 2. Thermal conductivity of pure fluids and mixtures," Ind. Eng. Chem. Fundam. **22**, 90 (1983).

[41]N. Zong and V. Yang, "An efficient preconditioning scheme for real-fluid mixtures using primitive pressure–temperature variables," Int. J. Comput. Fluid Dyn. **21**, 217 (2007).

[42]G. Soave, "Equilibrium constants from a modified Redlich–Kwong equation of state," Chem. Eng. Sci. **27**, 1197 (1972).

[43]G. Ribert, P. Domingo, and L. Vervisch, "Analysis of sub-grid scale modeling of the ideal-gas equation of state in hydrogen–oxygen premixed flames," Proc. Combust. Inst. **37**, 2345 (2019).

[44]P. E. Lapenna, G. Indelicato, R. Lamioni, and F. Creta, "Modeling the equations of state using a flamelet approach in LRE-like conditions," Acta Astronaut. **158**, 460 (2019).

[45]U. Guven and G. Ribert, "Impact of non-ideal transport modeling on supercritical flow simulation," Proc. Combust. Inst. **37**, 3255 (2019).

[46]H. Huo and and V. Yang, "Subgrid-scale models for large-eddy simulation of supercritical combustion," in *51st AIAA Aerospace Sciences Meeting Including the New Horizons Forum and Aerospace Exposition* (AIAA, 2013), p. 706.

[47]S.-Y. Hsieh and V. Yang, "A preconditioned flux-differencing scheme for chemically reacting flows at all Mach numbers," Int. J. Comput. Fluid Dyn. **8**, 31 (1997).

[48]R. C. Swanson and E. Turkel, "On central-difference and upwind schemes," J. Comput. Phys. **101**, 292 (1992).

[49]K. Hsieh, J. Shuen, and V. Yang, "Droplet vaporization in high-pressure environments I: Near critical conditions," Combust. Sci. Technol. **76**, 111 (1991).

[50]J. Shuen, V. Yang, and C. Hsiao, "Combustion of liquid-fuel droplets in supercritical conditions," Combust. Flame **89**, 299 (1992).

[51]N. Zong, H. Meng, S.-Y. Hsieh, and V. Yang, "A numerical study of cryogenic fluid injection and mixing under supercritical conditions," Phys. Fluids **16**, 4248 (2004).

[52]N. Zong and V. Yang, "Cryogenic fluid jets and mixing layers in transcritical and supercritical environments," Combust. Sci. Technol. **178**, 193 (2006).

[53]N. Zong and V. Yang, "Near-field flow and flame dynamics of LOX/methane shear-coaxial injector under supercritical conditions," Proc. Combust. Inst. **31**, 2309 (2007).

[54]X. Wang and V. Yang, "Supercritical mixing and combustion of liquid-oxygen/kerosene bi-swirl injectors," J. Propul. Power **33**, 316 (2017).

[55]X. Wang, H. Huo, Y. Wang, and V. Yang, "Comprehensive study of cryogenic fluid dynamics of swirl injectors at supercritical conditions," AIAA J. **55**, 3109 (2017).

[56]K. C. Gottiparthi, R. Sankaran, and, and J. C. Oefelein, "High fidelity large eddy simulation of reacting supercritical fuel jet-in-cross-flow using GPU acceleration," in *52nd AIAA/SAE/ASEE Joint Propulsion Conference* (AIAA, 2016), p. 4791.

[57]S. Yang, Y. Li, X. Wang, U. Unnikrishnan, V. Yang, and, and W. Sun, "Comparison of tabulation and correlated dynamic evaluation of real fluid properties for supercritical mixing," in *53rd AIAA/SAE/ASEE Joint Propulsion Conference* (AIAA, 2017), p. 4858.

[58]N. Peters, *Turbulent Combustion* (Cambridge University Press, Cambridge, 2000).

[59]X. Wang, H. Huo, and V. Yang, "Counterflow diffusion flames of oxygen and n-alkane hydrocarbons (CH_4-$C_{16}H_{34}$) at subcritical and supercritical conditions," Combust. Sci. Technol. **187**, 60 (2015).

[60]H. Huo, X. Wang, and V. Yang, "A general study of counterflow diffusion flames at subcritical and supercritical conditions: Oxygen/hydrogen mixtures," Combust. Flame **161**, 3040 (2014).

[61]J. Van Oijen, R. Bastiaans, G. Groot, and L. De Goey, "Direct numerical simulations of premixed turbulent flames with reduced chemistry: Validation and flamelet analysis," Flow, Turbul. Combust. **75**, 67 (2005).

[62]J. Van Oijen, R. Bastiaans, and L. De Goey, "Low-dimensional manifolds in direct numerical simulations of premixed turbulent flames," Proc. Combust. Inst. **31**, 1377 (2007).

[63]S. Mukhopadhyay, R. Bastiaans, J. van Oijen, and L. de Goey, "Analysis of a filtered flamelet approach for coarse DNS of premixed turbulent combustion," Fuel **144**, 388 (2015).

[64]C. Sung, C. K. Law, and J.-Y. Chen, *An Augmented Reduced Mechanism for Methane Oxidation with Comprehensive Global Parametric Validation* (Elsevier, 1998).